Technische Universität München
Fakultät für Physik

Abschlussarbeit im Masterstudiengang Physik

Positive Tensor Network Simulations of the Driven-Dissipative Bose-Hubbard Model

Xianrui Yin

02. December 2024

Erstgutachter (Themensteller): Prof. Dr. Peter Rabl
Zweitgutachter: Prof. Dr. Christian Mendl

Contents

Abstract

Open quantum systems have received significant attention recently due to their rich non-equilibrium phenomena and experimental advancements in quantum engineering. By engineering the coupling between the system and its environment, interesting quantum many-body states can be prepared. However, there are limited analytical results available in this field, and numerical simulations pose significant challenges due to the exponential increase in complexity with system size. In this thesis, we present a tensor network method for simulating the dynamics of open quantum systems governed by the Lindblad master equation. We represent the density matrix as a locally purified density operator and variationally compute its updates. By exploiting the degrees of freedom in the auxiliary space of the purification, we significantly reduced the complexity of the computations. To exemplify our method, we study a driven-dissipative Bose-Hubbard model with strong interactions— a parameter regime that was previously intractable. The model exhibits mean-field bistability. By simulating the Gutzwiller ansatz, we find that the system exhibits a first-order phase transition. The hysteresis area decays according to a power law in the fast sweep regime, while it shows an exponential decay in the slow sweep regime. In contrast, the simulation of the full density operator shows no first-order phase transition, and the dynamical hysteresis area decays exponentially only.

Acknowledgement

I would like to thank my supervisors, Prof. Dr. Peter Rabl and Prof. Dr. Christian Mendl, for their invaluable guidance, support, and encouragement throughout my research. Their expertise and insightful advice have been instrumental in shaping this thesis.

A special thanks to Dr. Xin Zhang for the many insightful discussions and for always providing thoughtful feedback that greatly enriched my understanding of the topic.

I would also like to extend my thanks to all those who have supported me, both academically and personally. Your encouragement and belief in me have made this achievement possible.

Chapter 1

Introduction

Since the advent of the density matrix renormalization group (DMRG) algorithm [1], tensor network methods have become state-of-the-art for studying low-dimensional quantum many-body systems. In one dimension, matrix product states effectively capture the area-law entanglement of ground states in gapped and local Hamiltonians. Algorithms like time evolution block decimation (TEBD) [2, 3] and the time-dependent variational principle (TDVP) [4] are widely used to simulate the time evolution of matrix product states governed by Schrödinger's equation. However, these methods are limited to pure states in a closed system. In reality, a system is never truly closed and continually interacts with its environment. Many efforts have been made to generalize tensor network techniques to simulate the evolution of mixed states for open quantum systems [5–7].

This task is particularly challenging for two main reasons. First, representing a density matrix for mixed states is computationally more demanding than simply using a state vector. Second, while numerous ansatzes have been proposed for pure states that are tailored to the area-law entanglement of underlying systems—allowing for efficient parameterization of the Hilbert space—certain laws governing mixed states do not exist, making it difficult to develop an efficient tensor network ansatz based on first principles.

One straightforward approach to represent the density matrix is to use a matrix product operator [5]. However, this method does not ensure that the density operator remains positive semi-definite under the time evolution. Another strategy involves purifying the density operator by extending it to a larger Hilbert space. In this context, a locally purified density operator has been proposed [6]. However, simulating this can become costly, as the dimension of the auxiliary Hilbert space may grow exponentially over time. In this work, we address this problem by exploiting the unitary degrees of freedom in the auxiliary space [8]. We demonstrate that this approach effectively mitigates the exponential growth of the auxiliary Hilbert space dimension, allowing for accurate simulations of the long-time dynamics of an open quantum system.

The thesis is organized as follows: In the first part, we will introduce key concepts related to quantum entanglement for both pure and mixed systems. We will also review essential elements of one-dimensional tensor networks.

In the second part, we will develop a numerical method to simulate the Markovian dynamics of an open quantum system using the locally purified density operator. This algorithm ensures that the density operator maintains unit trace and semi-definite positivity at all times. By employing a variational update of the tensor network, we can directly control the Frobenius norm error at each time step.

We demonstrate that we can achieve comparable results using significantly smaller bond dimensions by optimizing the basis for the auxiliary Hilbert space. Finally, we apply this method to investigate a driven-dissipative Bose-Hubbard model that exhibits mean-field bistability, revealing that bistability is disrupted due to quantum correlations.

Chapter 2

Fundamentals

In this chapter, we will review the key concepts of quantum entanglement and one-dimensional tensor networks, focusing on the difference between pure and mixed states.

2.1 Entanglement

Entanglement is one of the most peculiar characteristics of quantum mechanics, and it has no counterpart in classical mechanics. Measurements performed on a pair of entangled particles are correlated, even when the particles are separated by large distances. In the field of quantum information, entanglement is considered a valuable resource for information processing [9], with quantum teleportation being a notable example. On the other hand, entanglement also makes simulating many-body systems on classical computers very challenging.

In this section, we will introduce several key concepts related to quantum entanglement and relevant measures of entanglement for both pure states and mixed states. For a complete framework, see books [9, 10].

2.1.1 Pure states

Consider a composite quantum system $|\psi\rangle$ defined on the tensor product of two Hilbert spaces $\mathcal{H}_A$ and $\mathcal{H}_B$, that is

$$|\psi\rangle \in \mathcal{H}_A \otimes \mathcal{H}_B. \tag{2.1}$$

Given the orthonormal basis $|i\rangle_A$ and $|i\rangle_B$ for $\mathcal{H}_A$ and $\mathcal{H}_B$, respectively, the tensor products $|i\rangle_A \otimes |i\rangle_B$ form a basis for the tensor product space. A general quantum state can be expanded as

$$|\psi\rangle = \sum_{i,j} c^{i,j} |i\rangle_A |j\rangle_B, \tag{2.2}$$

where $c^{i,j}$ is a complex state vector with combined indices i, j. $|i\rangle_A|j\rangle_B$ is a short notation for $|i\rangle_A \otimes |i\rangle_B$, which we will repeatly use throughout the text.

By using Choi isomorphism $|i\rangle_A|j\rangle_B \to |i\rangle_A\ {}_B\langle j|$, we can naturally interpret the state vector $c^{i,j}$ as a matrix, such that $c^{i,j} = {}_A\langle i|c|j\rangle_B$ is the matrix element of some complex matrix $M \in \mathbb{C}^{\dim\mathcal{H}_A \times \dim\mathcal{H}_B}$ and has the following singular value decomposition,

$$c^{i,j} = u^{ik} s^{kk} v^{kj}, \tag{2.3}$$

where $\sum_k u^{ik} u^{*kj} = \delta^{ij}$ and $\sum_j v^{kj} v^{*ji} = \delta^{ki}$ are isometries and $s^{kl} = \delta_{kl} s_k$ is a diagonal matrix with non-negative real entries.

If we define a new basis $|\tilde{k}\rangle_A = u^{ik}|i\rangle_A$, $\langle\tilde{k}| = v^{*jk}\langle j|$, we can write the bipartite state in Eq. (2.2) under this new basis as

$$|\psi\rangle = \sum_{k}^{k_{max}} s_k |\tilde{k}\rangle_A |\tilde{k}\rangle_B, \tag{2.4}$$

where $k_{max} = \min(\dim(\mathcal{H}_A), \dim(\mathcal{H}_B))$.

We have expressed our state in a diagonal form by changing to a different basis in each subspace. This is known as the *Schmidt decomposition*. The orthonormal basis $|\tilde{k}\rangle_A$ and $|\tilde{k}\rangle_B$ are called *Schmidt bases*, s_k are called *Schmidt values* and are real and non-negative by the virtue of singular value decomposition. The normalization of the state $|\psi\rangle$ ensures that $\sum_k s_k^2 = 1$. The *Schmidt rank* is defined as the number of non-zero Schmidt values in Eq. (2.4).

A pure state $|\psi\rangle$ is called *separable* or *unentangled* if the Schmidt rank is 1. In other words, it can be written in the form of a product state

$$|\psi\rangle_S = |0\rangle_A \otimes |0\rangle_B. \tag{2.5}$$

The Schmidt decomposition also gives us a good handle to calculate the *reduced density matrix*, which is obtained by performing a partial trace over part of the system. Let ρ_A be the reduced density matrix on subsystem A,

$$\begin{aligned}
\rho_A &= \mathrm{Tr}_B\left(|\psi\rangle\langle\psi|\right) && (2.6)\\
&= \mathrm{Tr}_B\left(\sum_j\sum_k s_j s_k \left(|\tilde{j}\rangle_A \otimes |\tilde{j}\rangle_B\right)\left(\langle\tilde{k}|_A \otimes \langle\tilde{k}|_B\right)\right)\\
&= \sum_j\sum_k s_j s_k |\tilde{j}\rangle_{A,A}\langle\tilde{k}| \cdot {}_B\langle\tilde{k}|\tilde{j}\rangle_B\\
&= \sum_j\sum_k s_j s_k |\tilde{j}\rangle_{A,A}\langle\tilde{k}| \cdot \delta_{k,j}\\
&= \sum_j s_j^2 |\tilde{j}\rangle_{A,A}\langle\tilde{j}|. && (2.7)
\end{aligned}$$

If we measure some observable $\hat{O}_A$ which only acts on subsystem A, the result is given by

$$\begin{aligned}
\langle\hat{O}_A\rangle &= \mathrm{Tr}\left(\rho\left(\hat{O}_A \otimes \hat{I}_B\right)\right) && (2.8)\\
&= \mathrm{Tr}_A\mathrm{Tr}_B\left(\sum_j\sum_k s_j s_k \left(\hat{O}_A|\tilde{j}\rangle_A \otimes \hat{I}_B|\tilde{j}\rangle_B\right)\left(\langle\tilde{k}|_A \otimes \langle\tilde{k}|_B\right)\right)\\
&= \sum_j\sum_k s_j s_k {}_A\langle\tilde{k}|\hat{O}|\tilde{j}\rangle_A \cdot {}_B\langle\tilde{k}|\hat{I}|\tilde{j}\rangle_B\\
&= \sum_j s_j^2 {}_A\langle\tilde{j}|\hat{O}|\tilde{j}\rangle_A\\
&= \mathrm{Tr}_A\left(\rho_A\hat{O}_A\right), && (2.9)
\end{aligned}$$

where $\hat{I}_A$ denotes the identity operator on subsystem B.

This indicates that the measurements on part of the system are fully captured by its reduced density matrix. Furthermore, it enables us to quantify the amount of entanglement in our bipartite system, which can be expressed using the *Rényi entropy* as follows:

$$S_\alpha(\rho) = \frac{1}{1-\alpha}\log \mathrm{Tr}\rho_A^\alpha = \frac{1}{1-\alpha}\log \mathrm{Tr}\rho_B^\alpha \tag{2.10}$$

with $0 < \alpha < \infty$ and $\alpha \neq 1$. If we have obtained the Schmidt decomposition in Eq. (2.4), the equation above can be associated with the Schmidt values as:

$$S_\alpha = \frac{1}{1-\alpha} \log \left(\sum_k \left(s_k^2\right)^\alpha \right). \tag{2.11}$$

The two widely used entropy measures are the von Neumann entropy, which is obtained in the limit as $\alpha \to 1$:

$$\begin{aligned} S_{vN} &= -\mathrm{Tr}\left(\rho_A \log \rho_A\right) \\ &= -\mathrm{Tr}\left(\rho_B \log \rho_B\right) \\ &= -\sum_k s_k^2 \log(s_k^2), \end{aligned} \tag{2.12}$$

and the second Rényi entropy S_2, which takes the simpler form of the sum of quartic Schmidt values:

$$S_2 = -\sum_k \log(s_k^4). \tag{2.13}$$

For the case of a separable state as in Eq. (2.5), both S_{vN} and S_2 are equal to zero.

Recall that the entropy defined in thermodynamics is an extensive quantity. This also holds true for a general quantum state, meaning that the entropy scales with the system's size (volume) V. As shown in Ref. [11], a random state of a N-site system with local Hilbert space dimension d exhibits an entanglement entropy $S_{vN} \approx N/2 \log d - 1/2$, which scales with the system size N. This behavior is known as the *volume-law*.

Interestingly, a wide class of quantum states, specifically the ground states of local and gapped Hamiltonians, is conjectured to comply with the so-called *area law* of entanglement [12]:

$$S \sim A,$$

where A represents the area of the boundary when the system is divided into two parts. This phenomenon can be understood intuitively: when the Hamiltonian involves only local interactions, only the degrees of freedom near the boundary are entangled. For a one-dimensional system, this results in a constant bipartite entropy, $S \sim$ const, provided the system size exceeds the correlation length. The rigorous proof is given in Ref. [13].

We demonstrated the area law for the one-dimensional transverse field Ising model, given by the Hamiltonian:

$$\hat{H}_{Ising} = -J \sum_i \sigma_i^z \sigma_{i+1}^z - g \sum_i \sigma_i^x, \tag{2.14}$$

where σ_i^z and σ_i^x are Pauli operators acting on site i, J is the interaction strength between neighboring sites, and g is the strength of the transverse field. This model is known for exhibiting a quantum phase transition that occurs at $g/J = 1$.

In the thermodynamic limit for $g/J < 1$, the interaction terms dominate, and the system is in a symmetry-breaking phase with a magnetization of $\langle \sigma^z \rangle > 0$. Conversely, for $g/J > 1$, the system enters a symmetric phase where $\langle \sigma^z \rangle = 0$.

In Figure 2.1a, we present the von Neumann entropy S_{vN} for the ground states of the Hamiltonian in Eq. (2.14) for different values of g. These ground states are obtained using the DMRG algorithm [1]. As observed, for $g = 0.5$ and $g = 1.5$, S_{vN} exhibits a constant scaling with respect to system size. The jump in the $g = 0.5$ line occurs because symmetry breaking only manifests in the thermodynamic limit. Therefore, for finite systems, the ground state exists in a superposition of two symmetry-breaking states, resulting in an entropy of approximately $S \approx \log 2 \approx 0.69$. This is the case for $N < 40$ in Figure 2.1a. However, the entropy approaches zero for $N \geq 40$. This behavior is due to the two symmetry-breaking phases becoming degenerate at higher orders of g, causing the DMRG algorithm to identify either phase as the true ground state, leading to zero entanglement entropy.

At $g = 1$, the Hamiltonian in Eq. (2.14) becomes gapless, and the area law no longer applies; instead, it scales logarithmically with system size: $S \sim \log N$.

In Figure 2.1b, we present the Schmidt values at the boundary of the bipartite system. We observe a rapid decay in these values, which suggests that we can approximate the state in Eq. (2.4) by discarding the smaller Schmidt values:

$$|\psi\rangle = \sum_{k=1}^{D} s_k |\tilde{k}\rangle_A |\tilde{k}\rangle_B. \tag{2.15}$$

Here, D represents the number of Schmidt values retained in the approximation. As shown in Eq. (2.8), the measurement error resulting from the truncation is proportional to

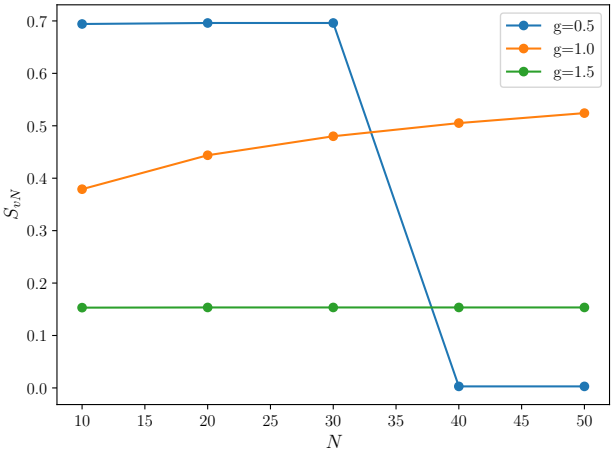

(a)

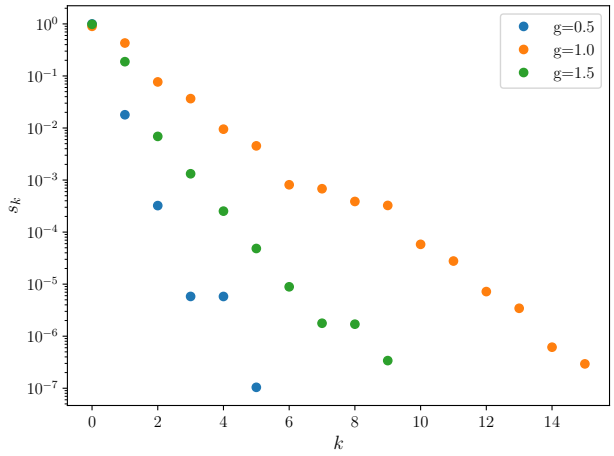

(b)

Figure 2.1: (a) The von Neumann entanglement entropy of ground states in a transverse field Ising model Eq. (2.14) with respect to the system size N, for different values of g. The system is split into two parts at its center. The interaction strength J is set to 1. For the case where $g = 0.5$, the entropy suddenly declines to almost 0 as the system size increases beyond 40. This occurs because the DMRG algorithm recognizes one of the symmetry-breaking states as the ground state, while the true ground state is actually a superposition of both states. The system becomes gapless at $g = 1$, and the entropy exhibits a logarithmic instead of constant scaling with the chain length. (b) The Schmidt values at the boundary exhibit rapid decay, making it possible to perform a truncation.

$$\sum_{k=D+1}^{k_{max}} s_k^2.$$

The matrix product states, which we will introduce later, effectively capture this behavior and offer an efficient parametrization for them.

2.1.2 Mixed states

In this section, we consider a mixed state for a bipartite system, which is described by a density operator defined on the tensor product space $\mathcal{H}_A \otimes \mathcal{H}_B$. Following the same notation used for the case of pure states, a general density operator can be written as

$$\rho = \sum_i w_i \left(\sum_j c^{i,j} |i\rangle_A |j\rangle_B \right) \left(\sum_k c^{*i,k} \langle i|_A \langle k|_B \right), \tag{2.16}$$

where w_i are classical probabilities which satisfy $\sum_i w_i = 1$ and $c^{i,j}$ are the complex coefficients that satisfy $\sum_j c^{i,j} c^{*i,j} = 1$.

A mixed state is called sparable if it can be written as a statistical mixture of unentangled pure states

$$\rho_S = \sum_i w_i \rho_A^i \otimes \rho_B^i. \tag{2.17}$$

For pure states, we have seen the von Neumann entanglement entropy S_{vN} in Eq. (2.12) provides a straightforward measure for the entanglement in the system, namely that the state is separable if and only if $S_{vN} = 0$. However, determining whether a mixed state is separable is a challenging task. In fact, solving the separability of a general bipartite state is proven to be NP-hard [14, 15].

One of the available entanglement measures for mixed states is the *entanglement of formation* [16, 17], which is defined as the average entropy of the pure states

$$E_f = \min \sum_i p_i S_{vN}(\psi_i), \tag{2.18}$$

where the minimization is over all the possible decompositions of ρ

$$\rho = \sum_i p_i |\psi_i\rangle\langle\psi_i|. \tag{2.19}$$

Such minimization problems are hard to solve analytically. For the special case of two qubits, the entanglement of formation can be given as an explicit function of ρ [17].

A similar quantity is *entanglement of purification* [18], which is defined through the purification of the density matrix ρ

$$E_p(\rho) = \min_{\psi:\mathrm{Tr}_B|\psi\rangle\langle\psi|=\rho} E_f(|\psi\rangle\langle\psi|), \tag{2.20}$$

while the minimization is over all the possible purifications. If ρ has a spectral decomposition $\rho = \sum_i \lambda_i |\psi_i\rangle\langle\psi_i|$, a general purification on a bipartite system defined on the Hilbert space $\mathcal{H}_A \otimes \mathcal{H}_B$ can be written as

$$|\psi\rangle = \sum_i \sqrt{\lambda_i} |\psi_i\rangle_{AB} \otimes |0\rangle_{A'} |i\rangle_{B'}, \tag{2.21}$$

where $|i\rangle_{A'}$ and $|i\rangle_{B'}$ being the basis of the auxiliary Hilbert space $\mathcal{H}_{A'}$ and $\mathcal{H}_{B'}$, respectively. The state ψ is a pure state in the extended Hilbert space $(\mathcal{H}_A \otimes \mathcal{H}_{A'}) \otimes (\mathcal{H}_B \otimes \mathcal{H}_{B'})$.

The density matrix is invariant under the unitary transforms $\hat{U}_{A'B'}$ acting on the auxiliary system A' and B'. Therefore, Eq. (2.20) can be rephrased as a minimization problem over all the unitary transformations

$$E_p(\rho) = \min_{\hat{U}_{A'B'}} S_{vN}\left(\left(\hat{I}_{AB} \otimes \hat{U}_{A'B'}\right)|\psi\rangle\langle\psi|\left(\hat{I}_{AB} \otimes \hat{U}^\dagger_{A'B'}\right)\right). \tag{2.22}$$

In Section 3.4, we will use an iterative algorithm to find such unitaries. We must note that the entanglement of purification Eq. (2.20) is indeed a correlation measure instead of an entanglement measure. It is proven in Ref. [19] that every correlated state will have a nonzero entanglement of purification, including those only having classical correlations. Since "the amount of quantum correlation in a state is smaller or equal to the total amount of correlation", the entanglement of purification is lower bounded by the entanglement of formation E_f.

2.2 Matrix product states

A quantum state describing a composite system containing L sites, is a vector $|\psi\rangle \in \mathcal{H}^{\otimes L}$, where $\mathcal{H}^{\otimes L}$ is defined as the tensor product of the single site Hilbert space $\mathcal{H}_k$ for $n = 1, 2, \ldots, L$

$$\mathcal{H}^{\otimes L} := \mathcal{H}_1 \otimes \mathcal{H}_2 \otimes \cdots \otimes \mathcal{H}_L.$$

Like in the bipartite case described in Section 2.1.1, we can construct a basis for this product Hilbert space by first specifying a local basis $\{|i_n\rangle\}$ for each site n, with i_n ranging from 1 to d_n, where $d_n = dim(\mathcal{H}_n)$ is the dimension of the local Hilbert space. The tensor product $|i_1\rangle \otimes |i_2\rangle \otimes \ldots \otimes |i_L\rangle$ then constitutes a basis for the Hilbert space of the full system. This is abbreviated as $|i_1, i_2, \ldots, i_L\rangle$. Therefore, a general quantum state can be written down as

$$|\psi\rangle = \sum_{i_1, i_2, \ldots, i_L} c^{i_1, i_2, \ldots, i_L} |i_1, i_2, \ldots, i_L\rangle, \tag{2.23}$$

where $c^{i_1, i_2, \ldots, i_L} \in \mathbb{C}^{\otimes L}$ is a rank-L tensor.

Matrix product states (MPS) are a special class of variational ansatz for quantum states, where the amplitudes in this tensor product basis are written as the contraction of the following local tensors

$$|\psi\rangle = \sum_{i_1, i_2, \ldots, i_L} A^{i_1}_{[1]} A^{i_2}_{[2]} \cdots A^{i_L}_{[L]} |i_1, i_2, \ldots, i_L\rangle, \tag{2.24}$$

$A^{i_n}_{[n]}$ are matrices of dimensions $D_n \times D_{n+1}$. D_k are called bond dimensions. If an open boundary condition is imposed, $D_1 = D_{L+1} = 1$. The subscript $[n]$ is the site index and indicates the matrices $A_{[k]}$ can be in general different. A graphic notation for a MPS is shown in Figure 2.2a, where each node is a tensor. The legs denote the indices of a tensor. Therefore, the number of the legs equals the rank of the tensor. The connected legs are contracted.

For any given quantum state Eq. (2.23), it is always possible to transform it into an MPS representation via successive singular value decomposition or QR decomposition. Following this procedure, a homogeneous system with local Hilbert space dimension d will result in a bond dimension $d^{L/2}$, which grows exponentially with the system size. However, as we have seen in Figure 2.1b, the Schmidt values of ground states of local and gapped Hamiltonians exhibit a fast decay. By discarding the small

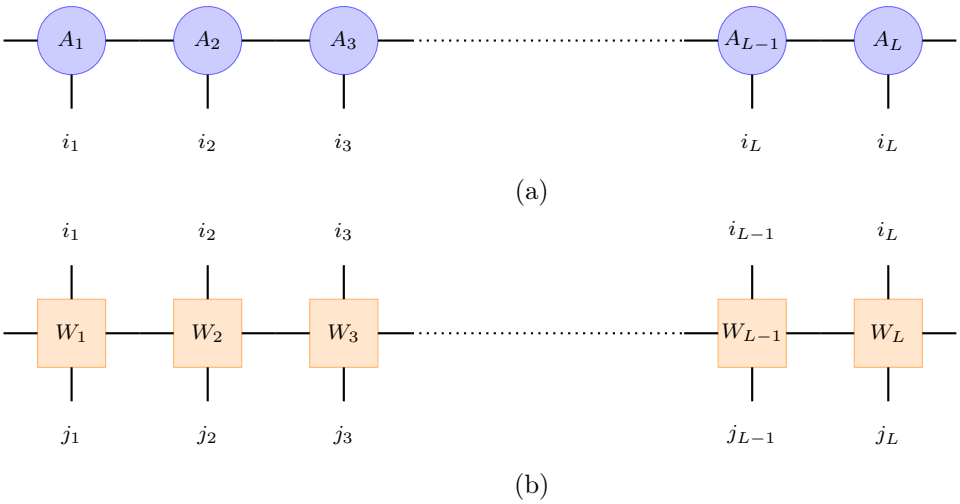

Figure 2.2: (a) A matrix product state (MPS). (b) A matrix product operator (MPO).

singular values, the bond dimensions can be significantly reduced, rendering MPS an efficient parametrization of the area law states.

2.3 Matrix product operators

A *matrix product operator* (MPO) for a one-dimensional system with L sites is given by:

$$\hat{O} = \sum_{\{i_n, j_n\}} W_{[1]}^{i_1 j_1} W_{[2]}^{i_2 j_2} \cdots W_{[L]}^{i_L j_L} |i_1, i_2, \ldots, i_L\rangle\langle j_1, j_2, \ldots, j_L|, \tag{2.25}$$

where $W_{[n]}^{i_n j_n}$ are matrices associated with the site k and the physical indices i_n, j_n. A graphical representation is given in Figure 2.2b. From now on, we will drop the subscript $[n]$ for simplicity.

MPO can be used to represent a large class of many-body operators, mostly known for local Hamiltonians. In the following, we will use MPO for other purposes, namely to represent the density operator and the time-evolution operator.

2.4 Locally purified density operator

Matrix product states discussed in Section 2.2 represent pure states in the many-particle Hilbert space. For a system that interacts with an environment, the quantum state is essentially a statistical mixture of pure states and is described by the density operator. One can represent the density operator as an MPO like in Eq. (2.25), often called a *matrix product density operator* (MPDO).

An MPDO must satisfy two conditions: it is positive semi-definite (P.S.D.) and has unit trace. However, positive semi-definiteness is a global property of the Hermitian operator. For a matrix product operator, it cannot be verified locally without contracting all components together [20]. Since truncations are necessary for most algorithms, maintaining positive semi-definiteness becomes challenging, even if the initial MPDO is constructed as a P.S.D. operator.

To address this issue, we can construct ρ as a Hermitian product, defined as

$$\rho = MM^\dagger \tag{2.26}$$

with

$$M = \sum_{\{i_n, j_n\}} X^{i_1 j_1} X^{i_2 j_2} \cdots X^{i_L j_L} |i_1, i_2, \ldots, i_L\rangle\langle j_1, j_2, \ldots, j_L|, \tag{2.27}$$

and M resembles a matrix product operator. $|i_1, i_2, \ldots, i_L\rangle$ is the basis for the physical Hilbert space with $1 \leq i_n \leq d_n$ and $|j_1, j_2, \ldots, j_L\rangle$ is the basis for the auxiliary Hilbert space with $1 \leq j_n \leq K_n$. Note that their dimensions d_n and K_n can differ from each other, though it is always sufficient to purify a density operator with $K_n = d_n$. This ansatz Eq. (2.26) is called a *locally purified density operator* (LPDO) [5, 6] and M is called the *purification operator*. An illustration of LPDO is provided in Figure 2.3.

In the following, we will refer to i_n as the *physical indices* and j_n as the *Kraus* or *auxiliary indices*, d_n as the *physical dimensions*, and K_n as the *Kraus* or *auxiliary dimensions*. The term "Kraus" is derived from the Kraus representation of the quantum channel, which we will introduce later.

The density matrix operator can thus be written as

$$\rho = \sum_{\{i_k, i'_k\}} A^{i_1 i'_1} A^{i_2 i'_2} \cdots A^{i_L i'_L} |i_1, i_2, \ldots, i_L\rangle\langle i'_1, i'_2, \ldots, i'_L| \tag{2.28}$$

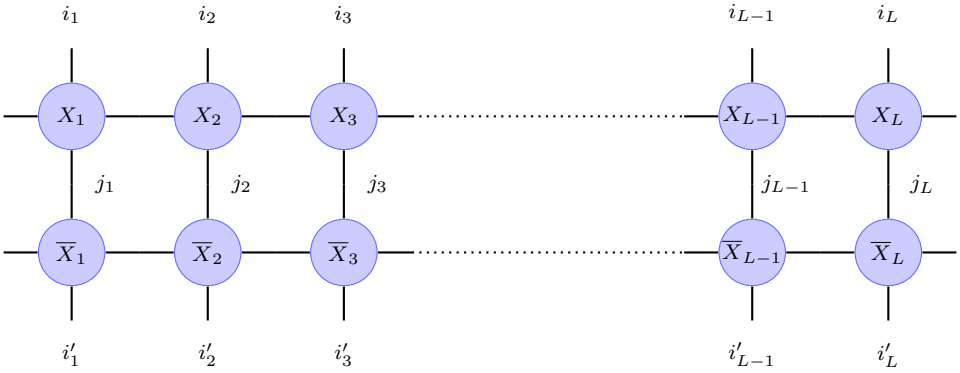

Figure 2.3: A locally purified density operator (LPDO)

with

$$A^{i_n,i'_n} = \sum_{j_n} X^{i_n j_n} \otimes \overline{X}^{i'_n j_n}, \tag{2.29}$$

as shown in Figure 2.3. $\overline{X}$ denotes the complex conjugate of X.

If we define an unnormalized MPS as

$$|\psi_{j_1,\cdots,j_L}\rangle = \sum_{i_1,\cdots,i_L} X^{i_1 j_1} X^{i_2 j_2} \cdots X^{i_L j_L} |i_1, i_2, \ldots, i_L\rangle, \tag{2.30}$$

the density operator in Eq. (2.28) can also be rephrased as

$$\begin{aligned} \rho &= \sum_{j_1,\cdots,j_L} |\psi_{j_1,\cdots,j_L}\rangle\langle\psi_{j_1,\cdots,j_L}| \\ &= \sum_k p_k |\tilde{\psi}_k\rangle\langle\tilde{\psi}_k|, \end{aligned} \tag{2.31}$$

where $k = j_1, \cdots, j_L$ is a collective index, $p_k = \langle\psi_k|\psi_k\rangle$ is the squared norm of $|\psi_k\rangle$ and $|\tilde{\psi}_k\rangle = |\psi\rangle/\sqrt{p_k}$.

In this form, the density operator represents an ensemble of pure MPS $|\tilde{\psi}_k\rangle$ with the corresponding probability p_k. If all the Krauss dimensions are trivial, Eq. (2.31) is reduced to a density matrix for a pure ensemble.

2.5 Canonical forms

In fact, the local tensors in MPS Eq. (2.24) and MPO Eq. (2.25) are not unique. The state or the operator remains the same if one inserts the identity $I = B^{-1}B$ between any pair of neighboring tensors. In this case, the B matrices only need to be left invertible and hence can be rectangular to increase the bond dimensions.

This gauge freedom allows us to define the canonical forms of MPS and MPO, which are essential for variational algorithms like DMRG and the algorithm we develop in the next chapter. An MPS is called is called *left* or *right canonical*, if all its local tensors satisfy the corresponding orthogonality conditions:

$$\sum_{i_k} (A^{i_k})^\dagger A^{i_k} = I \qquad \text{left canonical;} \tag{2.32a}$$

$$\sum_{i_k} A^{i_k} (A^{i_k})^\dagger = I \qquad \text{right canonical.} \tag{2.32b}$$

Similarly, we can define the canonical form for MPO by replacing the single sum with a double sum over both basis indices

$$\sum_{i_k, j_k} (W^{i_k, j_k})^\dagger W^{i_k, j_k} = I \qquad \text{left canonical;} \tag{2.33a}$$

$$\sum_{i_k, j_k} W^{i_k, j_k} (W^{i_k, j_k})^\dagger = I \qquad \text{right canonical.} \tag{2.33b}$$

We note that the canonical forms in Eq. (2.32) automatically ensure that the MPS has unit norm $\langle \psi | \psi \rangle = 1$ and for a purification operator, Eq. (2.33) gives to

$$\mathrm{Tr}\left(MM^\dagger\right) = 1. \tag{2.34}$$

Thus, the canonical forms enforce the unit trace condition of the density operator. If we define the inner product $\langle\langle \cdot | \cdot \rangle\rangle$ on the operator space as

$$\langle\langle A | B \rangle\rangle := \mathrm{Tr}\left(A^\dagger B\right), \tag{2.35}$$

the induced norm is called the *Frobenius norm*, denoted by $\| \cdot \|$

$$\|M\| := \sqrt{\langle\langle M | M \rangle\rangle}. \tag{2.36}$$

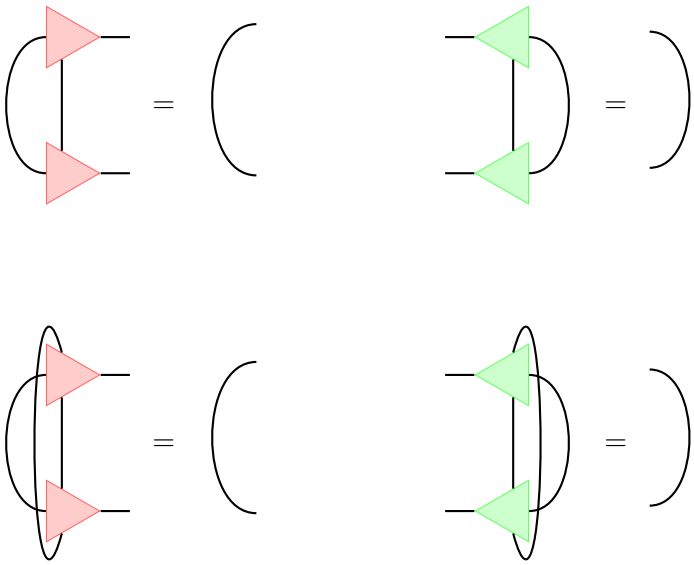

Figure 2.4: Top panel: left (right) orthonormal conditions Eq. (2.32) for MPS tensors on the left (right). Lower panel: left (right) orthonormal conditions Eq. (2.33) for MPO tensors on the left (right). The lines on the right-hand side of the equations represent the δ tensor.

The unit-trace condition in Eq. (2.34) for the density operator is then equivalent to the following unit norm condition of its purification operator

$$\|M\| = 1. \tag{2.37}$$

Note the Frobenius norm coincides with the usual 2-norm for vectors when the operator is vectorized. Therefore, $|M\rangle\rangle$ is also used to denote the vectorized form of an operator M.

The canonical forms are only a *partial* gauge fix of our MPS/MPO. There still exists a unitary degree of freedom on virtual connections. Eq. (2.32) and Eq. (2.33) still hold true if we insert $UU^\dagger$ between any neighboring matrices, where U is a unitary matrix. For the purification operator Eq. (2.27), this unitary degree of freedom also

exists on the auxiliary legs by noting that Eq. (2.29) is invariant if we apply a unitary transform on $|j_n\rangle$

$$W^{i_n,j'_n} = U_{j'_n,j_n} W^{i_n,j_n}. \tag{2.38}$$

This fact will become important for us later when we use this degree of freedom to remove entanglement from the locally purified density operator. We sometimes also refer to the Kraus indices (legs) as Kraus bonds, similar to the matrix bonds, to infer their artificial nature.

In practice, one can transform MPS (MPO) into right/left canonical form by performing successive QR decomposition starting from the boundary of the system [1]. Two other canonical forms are derived from the left and right canonical forms: the *mixed canonical form* and the *bond canonical form*. The first is particularly useful for calculating expectation values and correlation functions, while the second gives us back the Schmidt decomposition in the language of tensor networks.

As the name suggests, the mixed canonical form involves both the left and right orthonormal tensors. An MPS is mix-canonical if it is written as

$$|\psi\rangle = \sum_{i_1,i_2,\ldots,i_L} A^{i_1} \cdots A^{i_{j-1}} C^{i_j} A^{i_{j+1}} \cdots A^{i_L} |i_1, \ldots, i_L\rangle, \tag{2.39}$$

where C^{i_j} is called the *orthogonality center*. The matrices to the left of C^{i_j} are left orthonormal; meanwhile, those to the right of C^{i_j} are right orthonormal.

Similarly, the bond canonical form for MPS reads

$$|\psi\rangle = \sum_{i_1,i_2,\ldots,i_L} A^{i_1} \cdots A^{i_{j-1}} S_{[j]} A^{i_j} \cdots A^{i_L} |i_1, \ldots, i_L\rangle, \tag{2.40}$$

where $S_{[j]}$ is a diagonal matrix of dimension $D_j \times D_j$ and is called a *bond tensor*. A^{i_n} are left canonical for $n < j$ and right canonical for $n \geq j$. We write out the subscript explicitly here to emphasize that $C_{[j]}$ sits between site $j-1$ and j. We see that the bond canonical is exactly the Schmidt decomposition we have seen in Eq. (2.4), and the bond tensor (matrix) $S_{[j]}$ contains the Schmidt values.

The mixed canonical form and the bond canonical form can be defined similarly for the locally purified density operator. As shown in Figure 2.5, the bond canonical allows us to write down the following decomposition similar to the Schmidt decomposition

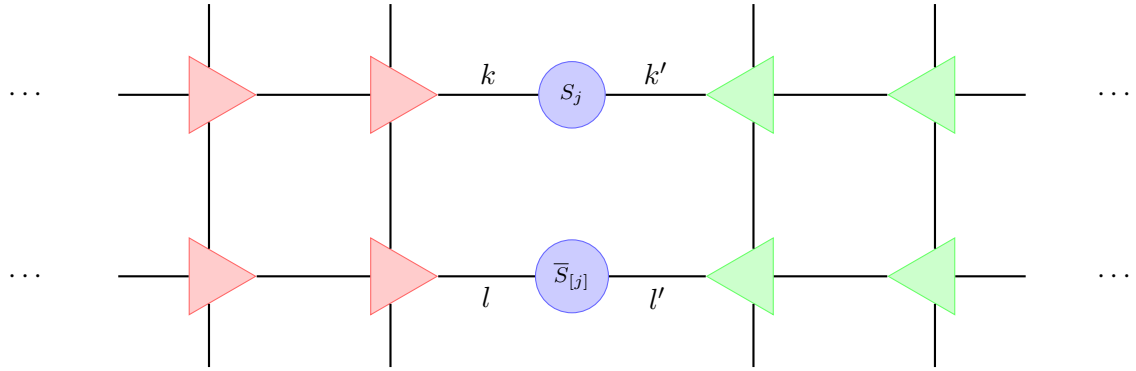

Figure 2.5: A LPDO in bond canonical form.

$$\begin{aligned}\rho &= \sum_{k,k'}\sum_{l,l'}\left(s_{k,k'}\delta^{k,k'}\right)\left(s_{l,l'}\delta^{l,l'}\right)\left(\rho_A^{k,l}\otimes\rho_B^{k',l'}\right)\\ &= \sum_{k,l} s_k s_l\left(\rho_A^{k,l}\otimes\rho_B^{k,l}\right)\\ &= \sum_k s_k^2\rho_A^k\otimes\rho_B^k + \sum_{k\neq l} s_k s_l\rho_A^{k,l}\otimes\rho_B^{k,l},\end{aligned} \tag{2.41}$$

where $s_{k,k'}$ is the matrix elements of the bond tensor $S_{[j]}$ and $\rho_A^{k,l}$ ($\rho_R^{k,l}$) corresponds to the network left (right) to the bond tensor. In the last line, we have separated the diagonal and off-diagonal terms. The orthonormal conditions in Eq. (2.33) translate into

$$\mathrm{Tr}\left(\rho_{A,B}^{k,l}\right) = \delta^{k,l} \qquad \text{and} \qquad \sum_k s_k^2 = 1. \tag{2.42}$$

Therefore, the first term in Eq. (2.41) represents a physical separable state, while the second term roughly tells us the entanglement in the system.

Last, we mention that even though we can follow the same recipe to define the canonical form for the matrix product density operator, it does not process the physical meanings we desire. In the "mixed canonical form", the MPDO reads

$$\rho = \sum_i \lambda_i \rho_A \otimes \rho_B. \tag{2.43}$$

It might be attempting to interpret the singular values λ_i as probabilities and ρ_A, ρ_B as density matrices on subsystems A and B. However, the orthogonality conditions is Eq. (2.33) do not guarantee us ρ_A or ρ_B to be positive semidefinite.

2.6 Lindblad Master equation

The dynamics of a closed system is described by the unitary time evolution operator

$$\hat{U}(t) = \exp\left(-i\hat{H}t\right), \tag{2.44}$$

where $\hat{H}$ is the Hamiltonian for the system. The density operator evolves according to Schrodinger's equation as

$$\rho(t) = \hat{U}(t)\rho(0)\hat{U}^{\dagger}(t). \tag{2.45}$$

More generally, the dynamics of a density operator ρ can be described by a *completely positive trace preserving* (CPTP) map $\mathcal{E}$

$$\mathcal{E} : \mathcal{H} \to \mathcal{H}, \qquad \rho \mapsto \mathcal{E}(\rho). \tag{2.46}$$

Trace preserving means that $\mathrm{Tr}(\mathcal{E}(\rho)) = \mathrm{Tr}\rho$, while completely positive means $\mathcal{E}\otimes\hat{I}_E$ is positive on any extension of the Hilbert space $\mathcal{H}\otimes\mathcal{H}_E$. This guarantees that when we apply $\mathcal{E}$ to a reduced density matrix on a composite system, the result density operator on the entire system remains a valid density operator. Furthermore, the map $\mathcal{E}$ is also linear and preserves hermicity.

By Choi's theorem [21], a CPTP map can always be expressed in the following form:

$$\mathcal{E}(\rho) = \sum_{i}^{K} V_i \rho V_i^{\dagger}, \tag{2.47}$$

where the following condition holds:

$$\sum_{i}^{K} V_i^{\dagger} V_i = \hat{I}. \tag{2.48}$$

Eq. (2.47) is also known as the *Kraus representation* of a quantum map. V_i are referred to as *Kraus operators*, K denotes the *Kraus rank* or *Kraus dimension*, and

it is important to note that $K < (\dim \mathcal{H})^2$. The same term, "Kraus dimension," was used before for the locally purified density operator introduced in Section 2.4. As we will see in the next chapter, these two quantities are related, which is why they share the same name.

In Eq. (2.45), $\hat{U}$ plays the role of the Kraus operators for the unitary dynamics, which does not change the purity of the system

$$\begin{aligned} \mathrm{Tr}\rho(t)^2 &= \mathrm{Tr}\left(\hat{U}(t)\rho(0)\hat{U}^\dagger(t)\hat{U}(t)\rho(0)\hat{U}^\dagger(t)\right) \\ &= \mathrm{Tr}\left(\hat{U}(t)\rho(0)^2\hat{U}^\dagger(t)\right) \\ &= \mathrm{Tr}\rho(0)^2. \end{aligned} \tag{2.49}$$

In the last line, we used the cyclic property of the trace. For an open quantum system coupled to some environment, a pure state can evolve into a mixed state due to the loss of information to the environment. We can ask if there exists a similar equation describing such non-unitary dynamics by considering a quantum map of an infinitesimal time δt

$$\rho(t+\delta t) = \sum_i V_i(t+\delta t)\rho(t)V_i^\dagger(t+\delta t), \tag{2.50}$$

where we have made the assumption that $\rho(t+\delta t)$ only depends on $\rho(t)$, meaning the dynamics is Markovian. This holds only if the correlation time between the system and the environment is much shorter than δt. In the limit of $\delta t \to 0$, the density operator remains unchanged with probability 1 and therefore a meaningful ansatz for the Kraus operators are

$$V_0 = \hat{I} + (\hat{K} - i\hat{H})\delta t\ , \qquad V_i = \hat{L}_i\sqrt{\delta t} \quad \text{for} \quad i > 0. \tag{2.51}$$

wher $\hat{H}$ and $\hat{K}$ are Hermitian operators. Eq. (2.48) requires that $2\hat{K} + \sum_i \hat{L}_i^\dagger \hat{L}_i = \mathcal{O}(\delta t^2)$

Therefore, Equation 2.50 translates into

$$\frac{d\rho}{dt} = -i\left[\hat{H}, \rho\right] + \sum_j \left(L_j\rho L_j^\dagger - \frac{1}{2}\left\{L_jL_j^\dagger, \rho\right\}\right). \tag{2.52}$$

This is known as the *Gorini–Kossakowski–Sudarshan–Lindblad equation (GKSL equation* [22–24], where $\hat{H}$ denotes the system Hamiltonian and $\hat{L}_j$ are called the *Lindblad (jump) operators*, which model the interaction with the environment. $\{A, B\} = AB + BA$ denotes the anti-commutator. In the following, we will refer to Eq. (2.52) Lindblad master equation.

A *nonequilibrium steady state* (NESS), denoted by $\rho_s s$, is defined as a fixed point of the Lindblad master equation, which satisfies

$$\frac{d}{dt}\rho_{ss} = 0. \tag{2.53}$$

It has been proven that for finite systems, there is always at least one steady state [25]. However, only a few models have been solved analytically [26, 27]. As a result, numerical methods are required to explore these systems further. In the next chapter, we will present a tensor network method to simulate the time evolution of a density operator governed by the Lindblad master equation.

Chapter 3

Algorithms

In this chapter, we will present a tensor network method to simulate the Lindblad master equation. We use a second-order Trotter splitting to approximate the time evolution operator. When the Lindblad operators only act on single sites, the unitary and dissipative dynamics can be handled separately. This is explained in Section 3.1. In Section 3.2, we will introduce a variational update scheme for the unitary dynamics. Section 3.3 will cover the implementation of the dissipative dynamics. Finally, in Section 3.4, we will present a disentanglement algorithm for the locally purified density operator and show it is the key to simulating long-time dynamics for many-body systems.

3.1 General Framework

The objective is to simulate the time evolution of the density operator according to the Lindblad master equation Eq. (2.52): $\frac{d\rho}{dt} = \mathcal{L}(\rho)$, where $\mathcal{L}$ is the Lindbladian superoperator living in the Hilbert space $\mathcal{H} \otimes \mathcal{H}$ and has the following matrix representation

$$\begin{aligned}\mathcal{L} &= -i(\hat{H} \otimes \hat{I} - \hat{I} \otimes \hat{H}^T) + \sum_j \left(\hat{L}_j \otimes \overline{\hat{L}}_j - (\hat{L}_j^\dagger \hat{L}_j \otimes \hat{I} + \hat{I} \otimes \hat{L}_j^T \overline{\hat{L}}_j)\right) \\ &= \mathbb{H} + \mathbb{D}.\end{aligned} \tag{3.1}$$

Here, $\overline{\hat{L}}_j$ and $\hat{L}_j^T$ denotes the complex conjugate and the transpose of an operator $\hat{L}_j$, respectively. Therefore, the adjoint operator of $\hat{L}_j$, denoted by $\hat{L}_j^\dagger$, equals to $\overline{\hat{L}_j^T}$. If $\mathcal{L}$ is time-independent, the time evolution of the density operator can be formally solved as

$$|\rho(t)\rangle\rangle = e^{\mathcal{L}t}|\rho(0)\rangle\rangle, \tag{3.2}$$

where $|\rho\rangle\rangle$ is the vectorized form of the density matrix ρ. For a small system, it is possible to compute the matrix exponential on the right-hand side to obtain the density matrix at any given time t. Consider a many-body system with N sites, where each site has a local Hilbert space dimension d. In this case, the density matrix will have a dimension of $d^N \times d^N$, and the corresponding Lindbladian as a matrix $\mathcal{L}$ will have a dimension of $d^{2N} \times d^{2N}$. Therefore, we need a quadratic amount of resources compared to the simulation of pure states.

Simulating the evolution of open quantum systems is an active area of research, with many methods proposed in the literature [5, 7, 28, 29]. These methods can be roughly divided into two categories. The first category includes ensemble (stochastic) methods, which simulate the evolution of many pure states and average over them, such as truncated Wigner approximation [30] and quantum jump method [31]. The second category includes those that tackle the density operator directly, such as simulating it as an MPO [5].

The choice of method depends on various factors related to the model, including its size, lattice dimensionality, local Hilbert space dimension, etc. For instance, the truncated Wigner method is particularly effective for large local Hilbert space dimensions where quantum fluctuations are minor and can be applied to systems of arbitrary lattice dimensions.

The tensor network method we develop in this work falls into the category of full quantum integration methods and operates in a complementary regime, accounting for full quantum fluctuations. We integrated Eq. (3.2) by representing the density operator in its locally purified form and discretizing the time evolution operator $e^{\mathcal{L}t} = \left(e^{\mathcal{L}\tau}\right)^N$, where N is the total time steps, and $\tau = t/N$ is the time step.

We consider a typical scenario where the Hamiltonian consists exclusively of two-local terms, given by:

$$\begin{aligned} \hat{H} &= \sum_n \hat{h}_{n,n+1} \\ &= \sum_{n \text{ is even}} \hat{h}_{n,n+1} + \sum_{n \text{ is odd}} \hat{h}_{n,n+1} \\ &= \hat{H}_e + \hat{H}_o \end{aligned} \tag{3.3}$$

and the Lindblad jump operators $\hat{L}_j$ act only on single sites. $\hat{H}_e$ ($\hat{H}_o$) includes the coupled terms between even-odd (odd-even) sites. The same notation follows below. We can use second-order Trotter splitting to approximate the evolution operator $e^{\mathcal{L}\tau}$ for a small time step τ as follows:

$$\begin{aligned} e^{\mathcal{L}\tau} &= e^{\mathcal{L}_e\tau/2}e^{\mathcal{L}_o\tau}e^{\mathcal{L}_e\tau/2} + \mathcal{O}(\tau^3) \\ &= e^{\mathbb{H}_e\tau/2}e^{\mathbb{H}_o\tau/2}e^{\mathcal{D}\tau}e^{\mathbb{H}_o\tau/2}e^{\mathbb{H}_e\tau/2} + \mathcal{O}(\tau^3). \end{aligned} \tag{3.4}$$

The state evolution, thereby, is

$$|\rho(t+\tau)\rangle\rangle \approx e^{\mathbb{H}_e\tau/2}e^{\mathbb{H}_o\tau/2}e^{\mathbb{D}\tau}e^{\mathbb{H}_o\tau/2}e^{\mathbb{H}_e\tau/2}|\rho(t)\rangle\rangle. \tag{3.5}$$

For simplicity, we will denote $\rho(t+\tau)$ as ρ' and omit explicit time arguments. This notation will also apply to the relevant time-dependent quantities we encounter, which should be clear from the context.

Since the operators in Eq. (3.5) are all completely positive, we can go to the Kraus representation introduced in Eq.(2.47), which is repeated below

$$\rho' = \sum_i V_i \rho V_i^\dagger. \tag{3.6}$$

3.2 Unitary dynamics

For unitary evolutions $e^{\mathbb{H}_\alpha\tau/2}$, the Kraus operators are just the unitary time evolution operator $\hat{U}_\alpha = e^{i\hat{H}_\alpha\tau/2}$, here $\alpha = o, e$. Eq. (3.6) becomes

$$\begin{aligned} e^{\mathbb{H}_\alpha\tau/2}|\rho\rangle\rangle &\to \hat{U}_\alpha\rho\hat{U}_\alpha^\dagger \\ &= \hat{U}_\alpha M M^\dagger \hat{U}_\alpha^\dagger \\ &= \left(\hat{U}_\alpha M\right)\left(\hat{U}_\alpha M\right)^\dagger \\ &= M'M'^\dagger \end{aligned} \tag{3.7}$$

with $M' = \hat{U}_\alpha M$.

We have presented the density operator in its locally purified form, as established in Section 2.4, using the purification operators M defined as follows:

$$M = \sum_{i_n, j_n} X^{i_1 j_1}_{m_1, m_2} X^{i_2 j_2}_{m_2, m_3} \cdots X^{i_L j_L}_{m_L, m_{L+1}} |i_1, i_2, \ldots, i_L\rangle\langle j_1, j_2, \ldots, j_L|. \tag{3.8}$$

In the above expression, the local tensors are denoted by X_n. Each X_n contains physical indices i_n, Kraus indices j_n, left matrix indices m_j, and right matrix indices m_{j+1}. Additionally, we can express the operator $\hat{U}_\alpha$ as a matrix product operator:

$$\begin{aligned}\hat{U}_\alpha &= e^{i\sum_n \hat{h}_{n,n+1}\tau/2} \\ &= \prod_n e^{i\hat{h}_{n,n+1}\tau/2} \\ &= \prod_n \hat{u}_{n,n+1}.\end{aligned} \tag{3.9}$$

As before, the summation is over the odd indices n when $\alpha = o$, and over the even indices when $\alpha = e$.

Since the operator $\hat{h}_{n,n+1}$ involves only two sites, $\hat{u}_{n,n+1}$ can be evaluated directly through Lanzcos algorithm or similar matrix exponential approximation algorithm. We can transform the resulting operator into an MPO acting on two-neighboring sites by singular value decomposition

$$\begin{aligned}\hat{u}_{n,n+1}^{[i_n,i'_n],[i_{n+1},i'_{n+1}]} &= U_{\omega_{n+1}}^{[i_n,i'_n]} S^{\omega_{n+1}} V_{\omega_{n+1}}^{[i_{n+1},i'_{n+1}]} \\ &= W_{\omega_n,\omega_{n+1}}^{i'_n n_1} W_{\omega_{n+1},\omega_{n+2}}^{i'_{n+1} i_{n+1}}.\end{aligned} \tag{3.10}$$

In the second line, we have defined $W_{\omega_n,\omega_{n+1}}^{i'_n n_1} = U_{\omega_{n+1}}^{[i_n,i'_n]}$ by introducing a dummy index ω_n, and set $W_{\omega_{n+1},\omega_{n+2}}^{i'_{n+1} i_{n+1}} = S^{\omega_{n+1}} V_{\omega_{n+1}}^{[i_{n+1},i'_{n+1}]}$ by introducing another dummy index ω_{n+2}. The index ω_{n+1} takes values from 1 to at most d^2 when the physical dimension is d. The indices grouped together in the square bracket are treated as a single index when performing the matrix decomposition.

This process is applied to every odd (even) number n for $\hat{U}_o$ ($\hat{U}_e$). Consequently, the matrix bond dimensions for $\hat{U}_o$ are d^2 between odd-even sites and 1 between even-odd sites, and vice versa for $\hat{U}_e$. Therefore, in the context of time evolution as per Eq. (3.5) and Eq. (3.7), it is typically recommended to first combine $\hat{U}_o$ and $\hat{U}_e$

$$\hat{U}_{o,e} = \hat{U}_o \hat{U}_e \tag{3.11}$$

before multiplying the result $\hat{U}_{o,e}$ with the purification operator M. For clarity, we will omit the subscripts o, e and e, o when there is no risk of confusion. The unitary MPO $\hat{U}$ is written as

$$\hat{U} = \sum_{i_n, i'_n} W^{i'_1 i_1}_{\omega_1,\omega_2} W^{i'_2 i_2}_{\omega_2,\omega_3} \cdots W^{i'_L i_L}_{\omega_L,\omega_{L+1}} |i'_1, i'_2, \cdots, i'_L\rangle\langle i_1, i_2, \cdots, i_n|. \tag{3.12}$$

The local tensor W_n from the unitary MPO therefore has the indices: i_n and i'_n for the physical legs, ω_j and ω_{j+1} for the matrix legs.

The time evolution is boiled down to multiplying the unitary operator $\hat{U}$ and the purification operator M. This can be done efficiently by using a variational approach to update our purification operator at every step by minimizing the distance between the M' and $\hat{U}M$

$$\begin{aligned} M' &= \arg\min_{M'} \|M' - \hat{U}M\| \\ &= \arg\min_{M'} \langle\langle M' - \hat{U}M | M' - \hat{U}M \rangle\rangle \\ &= \arg\min_{M'} \mathrm{Tr}\left(M'^{\dagger} M' - M'^{\dagger} \hat{U} M - M^{\dagger} \hat{U}^{\dagger} M' + \left(\hat{U}M\right)^{\dagger} \left(\hat{U}M\right) \right), \end{aligned} \tag{3.13}$$

where we have used the Frobenius norm defined Eq. (2.36). We can treat Eq. (3.13) as a variational problem involving local tensors $\overline{X}'_n$. Therefore, we require that the gradients with respect to $\overline{X}'_n$ vanish, leading to the equation:

$$\frac{\partial}{\partial \overline{X}'_n} \left(M'^{\dagger} M' - M'^{\dagger} \hat{U} M \right) = 0. \tag{3.14}$$

The last two terms in Eq. (3.13) drop out because they do not depend on $\overline{X}'_n$. The above expression is equivalent to

$$\frac{\partial}{\partial \overline{X}'_n} \left(M'^{\dagger} M' \right) = \frac{\partial}{\partial \overline{X}'_n} \left(M'^{\dagger} \hat{U} M \right). \tag{3.15}$$

We can translate Eq. (3.15) into tensor networks. Since both $M'^{\dagger}M'$ and $M'^{\dagger}\hat{U}M$ are linear in $\overline{X}'_n$, the partial derivative effectively removes $\overline{X}'_n$ from the graph. When M' is in mixed canonical form with the orthogonality center at site n, the left-hand side of Eq. (3.15) essentially corresponds to X'_n.

The right-hand side is more complicated and is illustrated in Figure 3.1. We can contract everything to the left of the site n into a left bond tensor $\mathbf{L}_n$, and everything to the right of the site n into a right bond tensor $\mathbf{R}_n$. Consequently, the entire

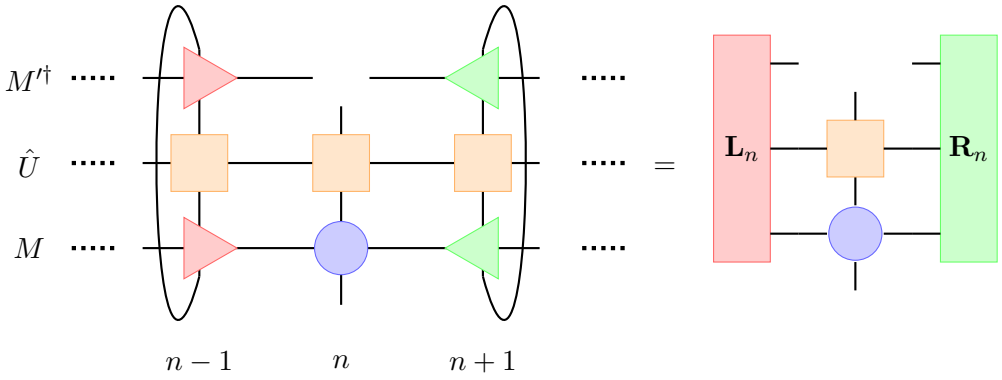

Figure 3.1: The right hand side of Eq. (3.15).

network consists of four components: the left bond tensor, the right bond tensor, W_n from the unitary MPO, and X_n from the purification operator M. We can optimize each X'_n by sweeping through the system, which resembles the procedure used in the DMRG algorithm.

It is important to note that the left and right bond tensors can be computed recursively. For example, we have $\mathbf{L}_{n+1} = ((\mathbf{L}_n X_n) W_n) X'_n$. This means we should store the bond tensors in memory and update them along with X'_n as we sweep through the system. The algorithm is described in Algorithm 1. As before, multiple dimensions are joined together when performing matrix decompositions for tensors with a rank higher than 2. The joined dimensions are grouped in a square bracket [ ]. Parenthesis ( ) indicates the optimal contraction sequence.

Similar to the DMRG algorithm, we can choose to optimize two neighboring sites together at each step, as outlined in Algorithm 2. A two-site tensor $\Theta_{n,n+1}$ is created by merging $X_n^{m_j,m_{j+1}}$ and $X_{n+1}^{m_{j+1},m_{j+2}}$. After contracting this tensor with the left and right bond tensors, we perform a truncated singular value decomposition as done in the one-site update. Singular values in S are truncated so that at most χ singular

values greater than ϵ are retained. In order to keep the unit-norm of the purification operator M', the truncation step is followed by renormalizing the singular values such that $\sum_k \tilde{s}^2 = 1$. The corresponding columns and rows of U and V are then discarded to obtain $\tilde{U}$ and $\tilde{V}$. The values of χ and ϵ need to be chosen such that the results converge.

In practice, we start with two-site updates to allow for adjustments to the bond dimensions. Once the maximum bond dimensions are reached, we switch to one-site updates, significantly speeding up the program.

Algorithm 1 One-Site Variational Update

Bring M into right canonical form.
Let the initial guess $M' = M$
Initialize the right bond tensors $\mathbf{R}_n$.
for $iter = 1$ to max_iter **do**
    for $n = 1$ to $L - 1$ **do**
        Compute the contractions in Fig. $X'_n \leftarrow ((\mathbf{L}_n W_n)\, X_n)\, \mathbf{R}_n$
        Compute the QR decomposition of X'_n:
            $X_n'^{[\sigma'_n,\mu'_n,m'_n],m'_{n+1}} = Q^{[\sigma'_n,\mu'_n,m'_n]} R^{m'_{n+1}}$
        Move orthogonality center to $n + 1$:
            $X'_n \leftarrow Q^{[\sigma',\mu',m'_n]}$ and $X'_{n+1} \leftarrow R^{m'_{n+1}} X'_{n+1}$
        Update the left bond tensors: $\mathbf{L}_{n+1} \leftarrow ((\mathbf{L}_n X_n)\, W_n)\, X'_n$
    end for
    for $n = L$ to 2 **do**
        Compute the contractions in Fig. $X'_n \leftarrow ((\mathbf{L}_n W_n)\, X_n)\, \mathbf{R}_n$
        Compute the RQ decomposition of X'_n:
            $X_n'^{m'_n,[\sigma'_n,\mu'_n,m'_{n+1}]} = R^{m'_n} Q^{[\sigma'_n,\mu'_n,m'_{n+1}]}$
        Move orthogonality center to $n - 1$:
            $X'_n \leftarrow Q^{[\sigma',\mu',m'_n]}$ and $X'_{n-1} \leftarrow X'_{n-1} R^{m'_{n-1}}$
        Update the right bond tensors: $\mathbf{R}_{n-1} \leftarrow \mathbf{R}_n W_n X_n X'_n$
    end for
    if convergence of the overlap $M'^{\dagger} \hat{U} M$ is achieved **then**
        break
    end if
end for
Output the final overlap and M'.

Algorithm 2 Two-Site Variational Update

Bring M into right canonical form.
Let the initial guess $M' = M$
Initialize the right bond tensors $\mathbf{R}_n$.
for $iter = 1$ to max_iter **do**
  for $n = 1$ to $L - 1$ **do**
    Compute the contractions $\Theta_{n,n+1} = ((((\mathbf{L}_n W_n) X_n) X_{n+1}) W_{n+1}) \mathbf{R}_{n+1}$
    Compute the singular value decomposition of $\Theta_{n,n+1}$:
      $\Theta_{n,n+1}^{[m'_n,\sigma'_n,\mu'_n],[m'_{n+2},\sigma'_{n+2},\mu'_{n+2}]} = U^{[m'_n,\sigma'_n,\mu'_n]} S V^{[m'_{n+2},\sigma'_{n+2},\mu'_{n+2}]}$
    Truncate and move orthogonality center to $n + 1$:
      $X'_n \leftarrow \tilde{U}^{[m'_n,\sigma'_n,\mu'_n]}$ and $X'_{n+1} \leftarrow \tilde{S}\tilde{V}^{[m'_{n+2},\sigma'_{n+2},\mu'_{n+2}]}$
    Update the left bond tensors: $\mathbf{L}_{n+1} \leftarrow ((\mathbf{L}_n X_n) W_n) X'_n$
  end for
  for $n = L$ to 2 **do**
    Compute the contractions $\Theta_{n-1,n} = ((((\mathbf{L}_n W_n) X_n) X_{n+1}) W_{n+1}) \mathbf{R}_n$
    Compute the singular value decomposition of $\Theta_{n,n+1}$:
      $\Theta_{n,n+1}^{[m'_n,\sigma'_n,\mu'_n],[m'_{n+2},\sigma'_{n+2},\mu'_{n+2}]} = U^{[m'_n,\sigma'_n,\mu'_n]} S V^{[m'_{n+2},\sigma'_{n+2},\mu'_{n+2}]}$
    Truncate and move orthogonality center to $n - 1$:
      $X'_n \leftarrow \tilde{U}^{[m'_n,\sigma'_n,\mu'_n]}\tilde{S}$ and $X'_{n+1} \leftarrow \tilde{V}^{[m'_{n+2},\sigma'_{n+2},\mu'_{n+2}]}$
    Update the right bond tensors: $\mathbf{R}_{n-1} \leftarrow \mathbf{R}_n W_n X_n X'_n$
  end for
  if convergence of the overlap $M'^{\dagger}\hat{U}M$ is achieved **then**
    break
  end if
end for
Output the final overlap and M'.

3.3 Dissipative Dynamics

Regarding the dissipative dynamics described by $e^{\tau\mathbb{D}}$ in Equation 3.5, when the Lindblad jump operators $\hat{L}_j$ are all single-site operators, this term factorizes

$$e^{\tau\mathbb{D}} = \otimes_n e^{\mathbb{D}_{[n]}\tau} \tag{3.16}$$

with

$$\mathbb{D}_{[n]} = \sum_j \left(\hat{L}_{[n],j} \otimes \overline{\hat{L}}_{[n],j} - (\hat{L}^{\dagger}_{[n],j}\hat{L}_{[n],j} \otimes \hat{I} + \hat{I} \otimes \hat{L}^{T}_{[n],j}\overline{\hat{L}}_{[n],j}) \right), \tag{3.17}$$

where $\hat{L}_{[n],j}$ is the j-th Lindblad jump operator that acts on site n.

In the next step, we find the Kraus operators in Equation 3.6 using Cholesky decomposition

$$e^{\mathcal{D}_{[n]}\tau} = \sum_{q_n=1}^{\tilde{K}_n} V_{[n],q_n} \otimes \overline{V}_{[n],q_n}, \tag{3.18}$$

where $\tilde{K}_n \leq d^2$ is the Kraus rank of the quantum map. It acts on site n as follows

$$\begin{aligned}
& e^{\mathcal{D}_{[n]}\tau} \left(\sum_{j_n=1}^{K_n} X_{[n],j_n} \otimes \overline{X}_{[n],j_n} \right) \\
&= \left(\sum_{q_n=1}^{\tilde{K}_n} V_{[n],q_n} \otimes \overline{V}_{[n],q_n} \right) \left(\sum_{j_n=1}^{K_n} X_{[n],j_n} \otimes \overline{X}_{[n],j_n} \right) \\
&= \sum_{q_n=1}^{\tilde{K}_n} \sum_{j_n=1}^{K_n} \left(V_{[n],q_n} X_{[n],j_n} \right) \otimes \left(\overline{V}_{[n],q_n} \overline{X}_{[n],j_n} \right) \\
&= \sum_{j'_n=1}^{\tilde{K}_n \cdot K_n} \left(X'_{[n],j'_n} \otimes \overline{X}'_{[n],j'_n} \right),
\end{aligned} \tag{3.19}$$

where q_n, j_n have been joined together to form a joint index j'_n of the updated local tensor $X'_{[n]}$. Therefore, the dissipative dynamics for a time step τ, is given by multiplying the Kraus operators $V_{[n],q_n}$ with $X_{[n],j_n}$ and joining the Kraus dimensions j_n and q_n. Eq. (3.19) also tells us that after a small time step τ, the Kraus dimension of the local tensors in the purification operator M are enlarged by a factor of $\tilde{K}_n$. Consequently, the Kraus bond dimensions will grow exponentially over time.

In Ref. [6], the Kraus dimensions are truncated through local basis transformation on the auxiliary Hilbert space $\{|j_n\rangle\}$ using the singular value decomposition

$$X_{j_n}^{[i_n,m_n,m_{n+1}]} = U_{j'_n}^{[i_n,m_n,m_{n+1}]} S^{j'_n} V_{j_n}^{j'_n}. \tag{3.20}$$

Similar to the case of truncating the matrix bond dimension, the Kraus bond dimension can be truncated by discarding the small singular values and setting a maximum Kraus bond dimension χ_K. The truncated matrices are $\tilde{U}$, $\tilde{S}$ and $\tilde{V}$ and we obtained local tensor

$$X_{j_n}^{[i_n,m_n,m_{n+1}]} = \tilde{U}_{j'_n}^{[i_n,m_n,m_{n+1}]} \tilde{S}^{j'_n}, \tag{3.21}$$

where we have left out the isometry $\tilde{V}$ because the density operator only depends on $\sum_{j_n} X_{j_n}^{i_n} \otimes X_{j_n}^{i'_n}$. Again, the truncated matrix $\tilde{S}$ must be renormalized to preserve the unit trace of the density operator.

The truncation recipes described in Eq. (3.20) and Eq. (3.21) are equivalent to a local basis transformation in the auxiliary Hilbert space on single sites, followed by discarding the states in Eq. (2.31) that have the lowest weights. It is evident that this approach is not optimal. A good purification ansatz should effectively consider the entire basis of the auxiliary Hilbert space. As we will demonstrate, this can result in large bond dimensions and/or significant truncation errors. An immediate improvement can be achieved by transitioning to a global basis optimization. In the next section, we will introduce a method to identify such a basis by minimizing the entanglement of the LPDO.

3.4 Disentanglement

At first glance, the exponentially growing (Kraus) bond dimensions make it impossible to study long-term dynamics. However, if the focus is solely on steady states, any errors that arise during the transient dynamics can be overlooked, as these deviations can be treated as specifying a new initial state.

As demonstrated in Ref. [6], simulating the steady states of a LPDO through time evolution requires large bond dimensions, both the matrix bond dimensions D and Kraus bond dimensions K. On the contrary, a variational approach that directly targets the steady state indicates that when the steady state is non-degenerate, the final state can often be represented by an MPDO with moderate matrix bond dimensions [28].

This suggests that the current representation of the density operator is inefficient, especially for steady states. The aim is to find a better representation of the density operator. Recall Eq. (2.31), the number of pure states in an LPDO is equal to the product of the dimensions of the auxiliary Hilbert spaces. Loosely speaking, a purification with a smaller overall Hilbert space dimension has, in general, less entanglement. This intuitive picture leads us to the entanglement of purification in Eq. (2.22), which is repeated below

$$E_p(\rho) = \min_{\hat{U}_{A'B'}} S_{vN}\left(\left(\hat{I}_{AB} \otimes \hat{U}_{A'B'}\right)|\psi\rangle\langle\psi|\left(\hat{I}_{AB} \otimes \hat{U}_{A'B'}^{\dagger}\right)\right) \tag{3.22}$$

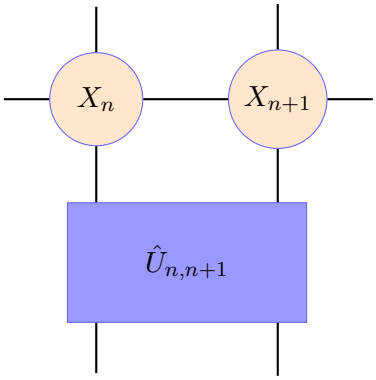

Figure 3.2: A two-site unitary acting on the auxiliary Hilbert space. Through unitary transformations in this two-site subspace, one can reduce the entanglement of the purification.

We hope that by minimizing the entanglement in the purification, in other words, *disentangling* the purification, we can reduce the dimensions of the auxiliary Hilbert space, which corresponds to the Kraus dimensions in the LPDO.

In Ref. [8], the authors proposed a disentanglement procedure to solve a similar problem, where the mixed state is purified by doubling the local Hilbert space on each site and represented as an MPS in the enlarged Hilbert space. This corresponds to fixing the Kraus dimension equal to the corresponding local Hilbert space's dimension and leaving only the matrix bond dimension as a variational parameter. Without dissipative dynamics, the matrix bond dimensions will still grow in a real-time evolution. The procedure was to find an MPS with a smaller matrix bond dimension through the following unitary transformations on the auxiliary Hilbert space

$$\hat{U}_{A'B'} = \hat{I}_0 \otimes \cdots \hat{I}_{n-1} \otimes \hat{U}_{n,n+1} \otimes \hat{I}_{n+2} \otimes \cdots \hat{I}_L \tag{3.23}$$

where $\hat{U}_{A'B'}$ is only nontrivial on sites $n, n+1$, shown in Figure 3.2.

The local optimization problem of finding $\hat{U}_{n,n+1}$ was then solved through an iterative method that determines the optimal $\hat{U}_{n,n+1}$ as a fixed point that minimizes the second Rényi entropy. The second Rényi entropy was chosen as the entanglement measure instead of the standard von Neumann entropy because it can be conveniently represented as a tensor network. The disentanglement procedure was completed by sweeping through the system to optimize all the bipartitions until a certain convergence criterion was satisfied.

The authors discovered that the disentanglement procedure could significantly reduce

entanglement during real-time evolution. However, it does not lead to a smaller matrix bond dimension due to the presence of a long tail in the Schmidt values in the MPS.

In our work, we implemented the same iterative optimizer to disentangle the LPDO. We would like to highlight two key differences in our work compared to previous research in Ref. [8]. First, the purification used there has always fixed Kraus dimensions due to the absence of dissipative dynamics. In contrast, our study considers both unitary and dissipative dynamics during real-time evolutions. As a result, both the matrix bond dimensions and Kraus bond dimensions increase over time. The entanglement of purification in Eq. (3.22) now depends on both parameters. Second, in our implementation, we have included an additional truncation step for the Kraus bonds, which we will explain further below.

In our simulations of a driven-dissipative Bose-Hubbard model (details in the next chapter), we observed a reduction in entanglement entropy after the disentanglement sweeps described above. As indicated in Ref. [8], this decrease does not lead to a reduction in the matrix bond dimensions D due to the long tail in the Schmidt values. In contrast, we found that the singular values associated with the Kraus bonds, $S^{j'_n}$ in Eq. (3.20), exhibit a sharp decline, with most of the weight concentrated in the first few singular values, while the remaining values are nearly zero. Consequently, we introduced a truncation of the Kraus dimensions, as specified in Eq. (3.21). In most scenarios, we found it possible to reduce the Kraus dimensions K down to the physical dimensions d.

This finding shows that by disentangling the purification process, we have found a more efficient parametrization of the LPDO, where the Kraus dimensions match the physical dimensions. However, it is important to note that this is still a local optimum. Theoretically, there is no evidence that an optimal purification in Eq. (2.20) will necessarily have the same Kraus dimensions as the physical dimensions. Further research is needed to explore the universality of this method for different systems.

In the example of a one-dimensional driven-dissipative Bose-Hubbard model, as detailed in Eq. (4.9), we compare the results of two different approaches. In the first approach, we applied only the local truncation methods described in Eq. (3.20) and Eq. (3.21). The results from this method are represented by the orange solid lines in Figure 3.3. In the second approach, we included a disentanglement procedure following each time step and applied the same local truncations afterward. The results from this method are shown by the green solid lines in Figure 3.3. The dynamics obtained without the disentanglement procedure significantly deviate from the correct dynamics, indicating that the chosen bond dimensions are insufficiently large. In contrast, by disentangling the LPDO after each time step, we achieve the correct dynamics using the same bond dimensions. The simulation results demonstrate that

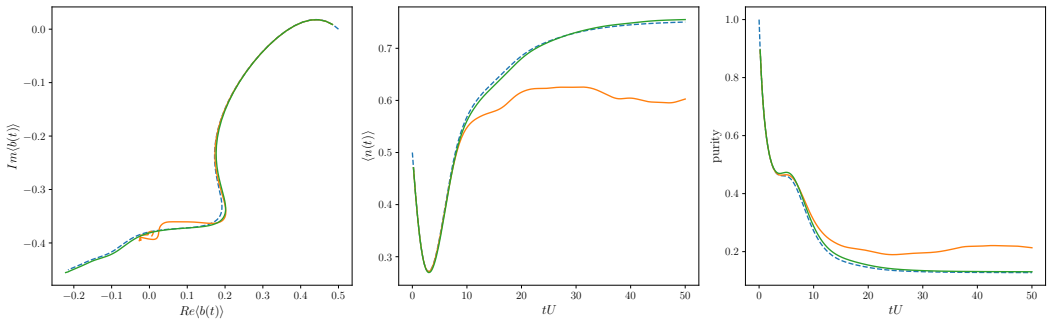

Figure 3.3: Simulation of a real-time evolution for a one-dimensional driven-dissipative Bose-Hubbard model Eq. (4.9) (introduced in the next chapter), with four sites numbered by $0, 1, 2, 3$. (a) The phase space trajectory of the time-dependent coherence $\langle b(t)\rangle$ for site 1. (b) The mean photon occupations $\langle n\rangle$ for site 1 as a function of time t (in units of U^{-1}). (c) The purity of the system as a function of time t (in units of U^{-1}). The dashed lines are obtained from direct integration of Eq. (3.2) and used as a reference. The green solid lines are obtained with our tensor network method, which includes a disentanglement procedure after each step. The orange solid lines are obtained using the same method but without disentanglement procedures. The bond dimensions in both simulations are $D = 8$ and $K = 8$. We observe that without the disentanglement procedure, the errors become substantial at large t due to truncation. The disentanglement procedure effectively reduces this error by truncating in an optimal basis of the auxiliary Hilbert space. The parameters for the driven-dissipative Bose-Hubbard model are chosen as follows: $J = 0.2$, $\mu = 0.2$, $F = 0.25$ and $\gamma = 0.3$, all in the units of U. The cutoff of the local Hilbert space dimension is set to 4.

the disentanglement procedure effectively eliminates the exponential growth of the Kraus bond dimensions in the LPDO representation while accurately capturing the long-time dynamics with a moderate bond dimension.

Chapter 4

The driven-dissipative Bose-Hubbard model

This chapter will employ the algorithm formulated in the previous chapter to study the driven-dissipative Bose-Hubbard model in one spatial dimension.

In Section 4.1, we will give a brief introduction to the driven-dissipative Bose-Hubbard model and existing results. Section 4.2 will provide a mean-field analysis of the model as a starting point. We find the system exhibits bistability by solving the Gross-Pitaveski mean-field equation. Subsequently, we take the single-site quantum effect into account by considering the Gutzwiller mean-field ansatz, which is also simple to simulate as a tensor network. There, we found the bistability is replaced with a first-order phase transition, different from the single-site analytical solution where no phase transitions occur. In the fast sweep regime, the dynamical hysteresis area exhibits a power-law decay, while in the slow sweep regime, it decays exponentially. Last, we present the tensor network simulation of the full density operator for this model. We find there is no first-order phase transition after a finite-size scaling. The dynamical hysteresis area exhibits an exponential decay only.

4.1 The model

We consider the coupled bosonic fields with nearest-neighbor interaction and coherent driving. Under the rotating-wave approximation, the Hamiltonian $\hat{H}$ is given by

$$\begin{aligned}\hat{H} = &\sum_j \left(\omega_j \hat{b}_j^\dagger \hat{b}_j + \frac{U}{2} \hat{n}_j (\hat{n}_j - 1) + F_j \left(\hat{b}_j e^{i\Omega_j t} + \hat{b}_j^\dagger e^{-i\Omega_j t} \right) \right) \\ &- \sum_{\langle i,j \rangle} J_{ij} \left(\hat{b}_i^\dagger \hat{b}_j + \hat{b}_j^\dagger \hat{b}_i \right),\end{aligned}$$

where ω_j is the energy for the j-th mode, here we have set $\hbar = 1$. $\hat{b}_j^\dagger$ and $\hat{b}_j$ are the boson creation and annihilation operators, $\hat{n}_j = \hat{b}_j^\dagger \hat{b}_j$ is the number operator. U_j is the interaction strength for a single mode, $J_{ij} = J_{ji}$ is the tunneling amplitude between different modes, $\langle i, j \rangle$ denotes the sum between nearest neighbors, F_j and Ω_j are the amplitude and the frequency of the coherent driving field, respectively.

When the system is coupled to a Markovian environment, the dynamics of the density matrix is described by the Lindblad master equation

$$\frac{d\rho}{dt} = -i[\hat{H}, \rho] + \mathcal{D}(\rho) \tag{4.1}$$

In the limit of zero environment temperature, the Lindblad dissipator $\mathcal{D}(\rho)$ describing only the boson losses is given by:

$$\mathcal{D}(\rho) = \sum_j \gamma_j \left(\hat{b}_j \rho \hat{b}_j^\dagger - \frac{1}{2} \{ \hat{b}_j^\dagger \hat{b}_j, \rho \} \right) \tag{4.2}$$

with γ_j being the dissipation rate of the j-th mode. $\{\cdot, \cdot\}$ denotes the anti-commutator.

This model can be used to describe a variety of open quantum systems. A well-known example is circuit quantum electrodynamics (QED) systems [32], where cavity photons interact through nonlinear effects. The dissipative dynamics account for photon leakage due to the finite lifetime of the photons, which is compensated by external pumping. An illustration of this is provided in Figure 4.1. Recently, large nonlinearities, where $U \gg \gamma$, have been achieved using superconducting quantum circuits [33]. This advancement made it possible to explore strong quantum effects in experimental settings.

It is often useful to move to a frame rotating at the driving frequency Ω_j. This transformation is achieved with the unitary operator:

$$\hat{U}(t) = \exp\left(i \sum_j \Omega_j \hat{b}_j^\dagger \hat{b}_j \, t \right). \tag{4.3}$$

The transformed Hamiltonian $\hat{H}'$ in the rotating frame is:

$$\hat{H}' = \hat{U} \hat{H} \hat{U}^\dagger - i \hat{U} \frac{\partial \hat{U}^\dagger}{\partial t}. \tag{4.4}$$

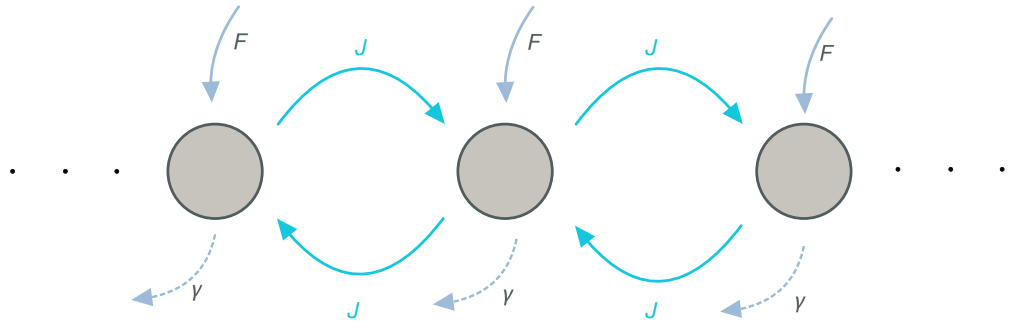

Figure 4.1: An illustration fo the driven-dissipative Bose-Hubbard model. The meaning of the parameters are explained in the main text.

An extra time-derivative term arises because the unitary operator is time-dependent. This term evaluates to:

$$-i\hat{U}\frac{\partial\hat{U}^\dagger}{\partial t} = -i\hat{U}\hat{U}^\dagger\left(-i\sum_j \Omega_j \hat{b}_j^\dagger \hat{b}_j\right) = -\sum_j \Omega_j \hat{b}_j^\dagger \hat{b}_j. \tag{4.5}$$

To obtain the first term $\hat{U}\hat{H}\hat{U}^\dagger$, we only need to calculate how the unitary operator $\hat{U}(t)$ acts on the annihilation operator $\hat{b}_j$

$$\hat{U}(t)\,\hat{b}_j\,\hat{U}^\dagger(t) = e^{i\Omega_j\hat{n}_j t}\,\hat{b}_j\,e^{-i\Omega_j\hat{n}_j t} = \hat{b}_j e^{-i\Omega_j t} \tag{4.6}$$

Similarly, we have

$$\hat{U}(t)\,\hat{b}_j^\dagger\,\hat{U}^\dagger(t) = \hat{b}_j^\dagger e^{i\Omega_j t}. \tag{4.7}$$

Thus, in the rotating frame, the exponents in the driving terms cancel out

$$\hat{b}_j e^{i\Omega_j t} \to \left(\hat{b}_j e^{-i\Omega_j t}\right) e^{i\Omega_j t} = \hat{b}_j,$$
$$\hat{b}_j^\dagger e^{-i\Omega_j t} \to \left(\hat{b}_j^\dagger e^{i\Omega_j t}\right) e^{-i\Omega_j t} = \hat{b}_j^\dagger.$$

The diagonal terms $\hat{b}_j^\dagger \hat{b}_j$ are invariant under this transformation, the on-site energy term $\sum_j \omega_j \hat{b}_j^\dagger \hat{b}_j$ effectively shifts by $-\sum_j \Omega_j \hat{b}_j^\dagger \hat{b}_j$ due to Eq. (4.5), resulting in:

$$\sum_j (\omega_j - \Omega_j) \hat{b}_j^\dagger \hat{b}_j = -\sum_j \mu_j \hat{b}_j^\dagger \hat{b}_j,$$

where $\mu_j = \Omega_j - \omega_j$ is the detuning between the driving frequency and the cavity frequency.

If we assume that the driving frequency Ω_j is identical for every site j, the Hamiltonian Eq. (4.4) becomes:

$$\begin{aligned} \hat{H}' = &\sum_j \left(\frac{U}{2} \hat{n}_j (\hat{n}_j - 1) - \Delta_j \hat{b}_j^\dagger \hat{b}_j + F_j (\hat{b}_j + \hat{b}_j^\dagger) \right) \\ &- J \sum_{\langle i,j \rangle} \left(\hat{b}_i^\dagger \hat{b}_j + \hat{b}_j^\dagger \hat{b}_i \right), \end{aligned} \tag{4.8}$$

where each term is now time-independent, with the detuning μ_j and the constant drive term $F_j(\hat{b}_j + \hat{b}_j^\dagger)$ representing the coherent drive in the rotating frame.

In this work, we consider the situation where the system is homogeneous, that all cavities are identical, and the external driving field is the same for each cavity. The Hamiltonian now reads

$$\hat{H} = \sum_j -\mu \hat{b}_j^\dagger \hat{b}_j + \frac{U}{2} \hat{b}_j^\dagger \hat{b}_j^\dagger \hat{b}_j \hat{b}_j - J(\hat{b}_{j+1}^\dagger \hat{b}_j + \hat{b}_j^\dagger \hat{b}_{j+1}) + F(\hat{b}_j^\dagger + \hat{b}_j) \tag{4.9}$$

The Bose-Hubbard model for a closed system without external drive and dissipation is known for a superfluid-Mott insulator phase transition at zero temperature. In the limit of large interaction strength U, the system is a Mott insulator. When the ratio between the tunneling amplitude J and the interaction strength U is increased, the system experiences a second-order phase transition by breaking the $U(1)$ symmetry. The resulting superfluid phase has a long-range order and zero viscosity.

In our model Eq. (4.9), the $U(1)$ symmetry is explicitly broken by the external driving. Thus, such a transition will not occur.

Similar to a quantum phase transition at zero temperature, where the competition between non-commuting terms in the Hamiltonian can cause abrupt changes in the

ground state, the competition between unitary and dissipative dynamics in the Lindblad master equation can lead to abrupt changes in the nonequilibrium steady state, giving rise to a dissipative quantum phase transition [34, 35].

The driven-dissipative Bose Hubbard model described in Eq. (4.9) turns out to have a very rich phase diagram. In Ref. [36], the author solved a self-consistent mean-field equation using the single-site analytical solution. It was found that the system exhibits bistability, namely, that it has two steady states in a finite range of parameters.

It is widely believed certain bistability is only an artifact of the mean-field theory and is replaced by a first-order phase transition when quantum fluctuations are taken into consideration. Such dissipative phase transition is oberserved in experiment for a 1D circuit QED array driven at one end [37].

In Ref. [38], the author simulated both 1D and 2D models with truncated Wigner approximation and found the Liouvillian gap converges to a finite value in the 1D case after finite-size scaling; thus, no phase transition happens.

We want to point out that the previous works we discussed above mostly close to the semi-classical case, where the interaction U is weak. In this regime, the system has high occupation numbers and quantum fluctuations are negligible, the mean-field theory and truncated Wigner approxiation therefore provide a good description of the system.

The strong quantum limit, on the other hand, is not well studied due to the limit of existing numerical methods. In the following, we will use the time evolution algorithm developed in the last chapter to study the driven-dissipative Bose-Hubbard model and compare it to the results obtained from the Gross-Pitaevski mean-field equation and Gutzwiller mean-field equation. To highlight the strong interaction regime we are focusing on, the model parameters we used in numerical simulations are defined in the unit of the interaction strength U by setting $U = 1$. The tunneling amplitude J, the driving amplitude F and the dissipation rate γ are 0.2, 0.25, 0.3, respectively.

It is worth noting that a more common practice is to define the parameters in units of γ, as it determines the relaxation time. However, since γ remains constant across all our simulations, this choice of units does not affect our results.

4.2 Mean-field theory analysis

The Heisenberg equation of motion for the annihilation operator $\hat{b}_i$ reads

$$\dot{\hat{b}}_i = -i\left[\hat{b}_i, \hat{H}\right] + \gamma\left(\hat{b}_i^\dagger \hat{b}_i \hat{b}_i - \frac{1}{2}\left\{\hat{b}_i^\dagger \hat{b}_i, \hat{b}_i\right\}\right). \tag{4.10}$$

Using the commutator relations

$$[\hat{b}_i^\dagger, \hat{b}_j^\dagger] = [\hat{b}_i, \hat{b}_j] = 0, \quad [\hat{b}_i, \hat{b}_j^\dagger] = \delta_{ij}, \tag{4.11}$$

the first commutator equals to

$$\begin{aligned}
[\hat{b}_i, \hat{H}] &= -\mu[\hat{b}_i, \hat{b}_i^\dagger \hat{b}_i] + \frac{U}{2}[\hat{b}_i, \hat{b}_i^\dagger \hat{b}_i^\dagger \hat{b}_i \hat{b}_i] - J[\hat{b}_i, \hat{b}_i^\dagger \hat{b}_{i-1} + \hat{b}_i^\dagger \hat{b}_{i+1}] + F[\hat{b}_i, \hat{b}_i^\dagger] \\
&= -\mu \hat{b}_i + \frac{U}{2}(\hat{b}_i \hat{b}_i^\dagger \hat{b}_i^\dagger \hat{b}_i \hat{b}_i - \hat{b}_i^\dagger \hat{b}_i^\dagger \hat{b}_i \hat{b}_i \hat{b}_i) - J(\hat{b}_{i-1} + \hat{b}_{i+1}) + F \\
&= -\mu \hat{b}_i + U \hat{b}_i^\dagger \hat{b}_i \hat{b}_i - J(\hat{b}_{i-1} + \hat{b}_{i+1}) + F.
\end{aligned} \tag{4.12}$$

Similarly, the dissipative terms equals to $\frac{\gamma}{2}(\hat{b}_i^\dagger \hat{b}_i \hat{b}_i - \hat{b}_i \hat{b}_i^\dagger \hat{b}_i) = -\frac{\gamma}{2}\hat{b}_i$. Combining the coherent evolution and the dissipative dynamics, we arrive at

$$\dot{\hat{b}}_i = -i\left(-\mu \hat{b}_i + U \hat{b}_i^\dagger \hat{b}_i \hat{b}_i - J\left(\hat{b}_{i-1} + \hat{b}_{i+1}\right) + F\right) - \frac{\gamma}{2}\hat{b}_i. \tag{4.13}$$

Due to the presence of the nonlinear term, we cannot solve this equation analytically. A standard approach is using mean-field theory, starting by replacing the operator with its mean-field value $\beta_i = \langle \hat{b}_i \rangle$ and using $\langle \hat{b}_i^\dagger \hat{b}_i \hat{b}_i \rangle \approx |\beta_i|^2 \beta_i$ under the mean-field approximation, we obtain the so-called Gross-Pitaevski mean-field equation of motion for β_i,

$$\frac{d\beta_i}{dt} = i\left(\mu\beta_i - U|\beta_i|^2\beta_i + J\left(\beta_{i-1} + \beta_{i+1}\right) - F\right) - \frac{\gamma}{2}\beta_i. \tag{4.14}$$

This is a system of equations for β_i. Define a vector $\boldsymbol{\beta} = (\beta_1, \beta_2, \ldots, \beta_N)$ (for a system of size N). In the steady state, $\frac{d\boldsymbol{\beta}}{dt} = 0$:

$$\begin{pmatrix} u_1 & J & & \\ J & u_2 & & \\ & & \ddots & \\ & & J & u_N \end{pmatrix} \begin{pmatrix} \beta_1 \\ \beta_2 \\ \vdots \\ \beta_N \end{pmatrix} - F = 0, \tag{4.15}$$

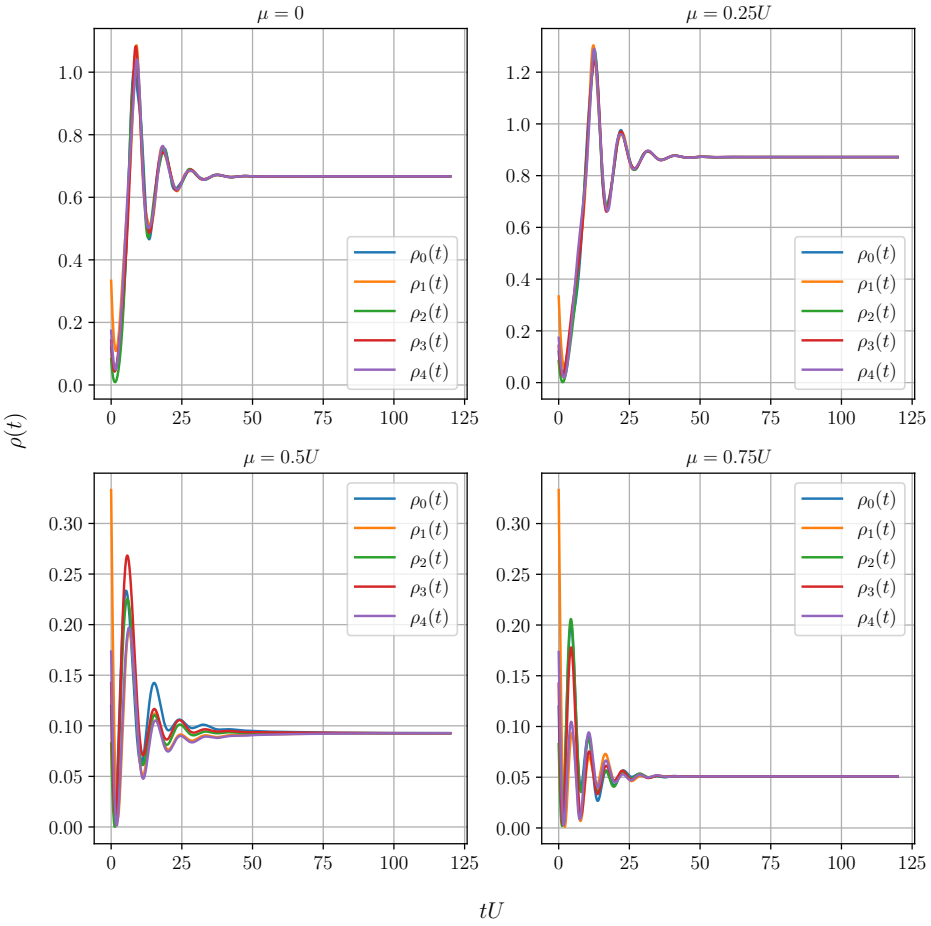

Figure 4.2: The time-dependent mean-field photon density $\rho(t)$ on every site for an array of 5 sites, numbered by $0, 1, 2, 3, 4$, for different detunings μ. The trajectories are obtained by numerical integration of Eq. (4.14) using a fourth-order Runge-Kutta method. The initial conditions are chosen such that the cavity array has inhomogeneous occupations. The rest of the parameters are $F = 0.25U$, $\gamma = 0.3U$, $J = 0.2U$. In all cases, we found that the steady-state configurations were homogeneous.

where $u_i = \mu - U|\beta_i|^2 + i\frac{\gamma}{2}$ and open boundary conditon is assumed.

Since we do not assume that the system is homogeneous, the diagonal entries of our tridiagonal matrix can be different. Therefore, it is not possible to solve the matrix equation analytically. Instead, we simulate the time dependence of the mean fields β_i using different initial conditions. We know the system has reached a steady state once the values of β_i become stationary.

We utilize the fourth-order Range-Kutta method to integrate the differential equations Eq. (4.14). We assume a periodic boundary condition such that $\beta_{N+1} = \beta_1$ and $\beta_0 = \beta_N$. In Figure 4.2 we show a number of sample trajectories. We have defined the mean-field photon density as $\rho_i = |\beta_i|^2$. It is important to note that this should not be confused with the density operator that we will encounter in the next section. Our findings indicate that, in all cases, the system relaxes to a homogeneous configuration. The outcome is expected due to the translational invariance of our model. Consequently, we can assume a homogeneous solution, namely $\langle \hat{b}_i \rangle$ is the same for all i, Eq. (4.14) reduces to a scalar equation,

$$\left(\tilde{\mu} - U|\beta|^2 + i\frac{\gamma}{2}\right)\beta = F. \tag{4.16}$$

Here we have dropped the subscript i and define $\tilde{\mu} = \mu + 2J$. Taking the magnitude on both sides and solving for ρ:

$$U^2\rho^3 - 2U\tilde{\mu}\rho^2 + (\tilde{\mu}^2 + \frac{\gamma^2}{4})\rho - F^2 = 0. \tag{4.17}$$

Divide the equation by U^2, which is equivalent to redefining the rest of the parameters in the unit of U, we get

$$\rho^3 - 2\tilde{\mu}\rho^2 + (\tilde{\mu}^2 + \frac{\gamma^2}{4})\rho - F^2 = 0. \tag{4.18}$$

This is a cubic equation in terms of ρ, and we are interested in determining how many positive real roots it has, which correspond to the density of the mean-field steady states. To answer this question, we can start by examining the discriminant.

The discriminant of a general cubic polynomial $p_3(x) = ax^3 + bx^2 + cx + d$ is defined as

$$\Delta = 18abcd - 4b^3d + b^2c^2 - 4ac^3 - 27a^2d^2.$$

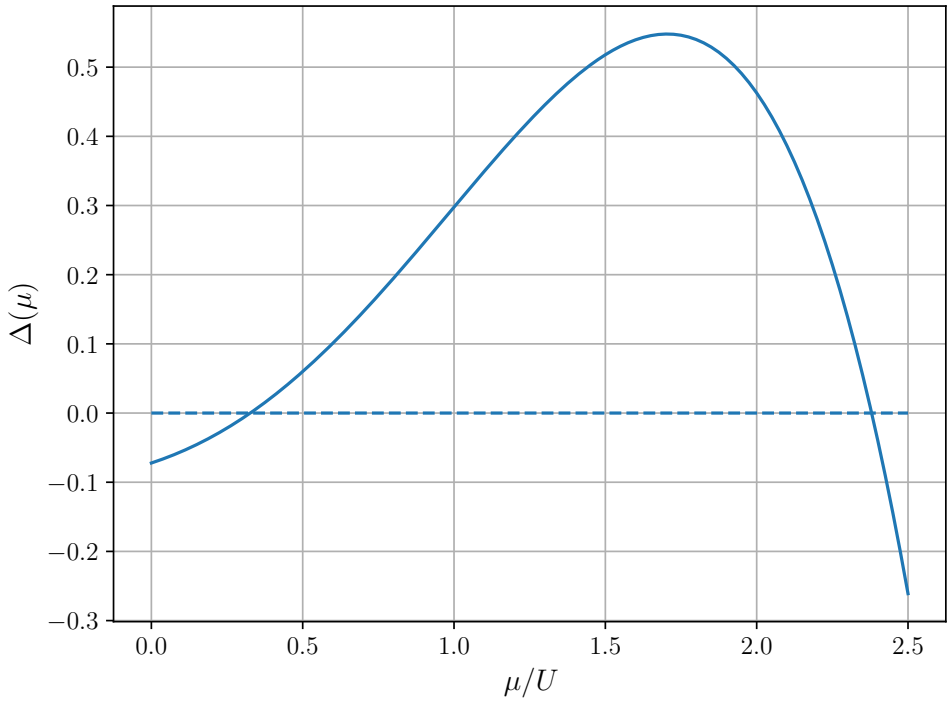

Figure 4.3: The discriminant Δ of $G(\rho)$ as a function of μ. $\Delta > 0$ means there are three distinct real roots. $\Delta < 0$ means there are one real root and two complex conjugate roots. The model parameters defining the discriminant are the same as in Figure 4.2.

We refer to the left-hand side of Eq. (4.18) as $G(\rho)$, the coefficients a, b, c, d are given as:

$$a = 1, \quad b = -2\tilde{\mu}, \quad c = \tilde{\mu}^2 + \frac{\gamma^2}{4}, \quad d = -F^2.$$

If we consider the discriminant as a function of the detuning μ, the polynomial $G(\rho)$ will have three distinct real roots if $\Delta(\mu) > 0$. Conversely, if $\Delta(\mu) < 0$, $G(\rho)$ will have one real root along with a pair of complex conjugate roots. When $\Delta(\mu)$ equals zero, $G(\rho)$ will have degenerate roots.

The sign of $\Delta(\mu)$ can be determined by first plotting the function, as illustrated in Figure 4.3. By employing a numerical root-finding method, such as the bisection search, we identify the numerical values of the two roots of $G(\rho)$, which are $\mu_1 =$

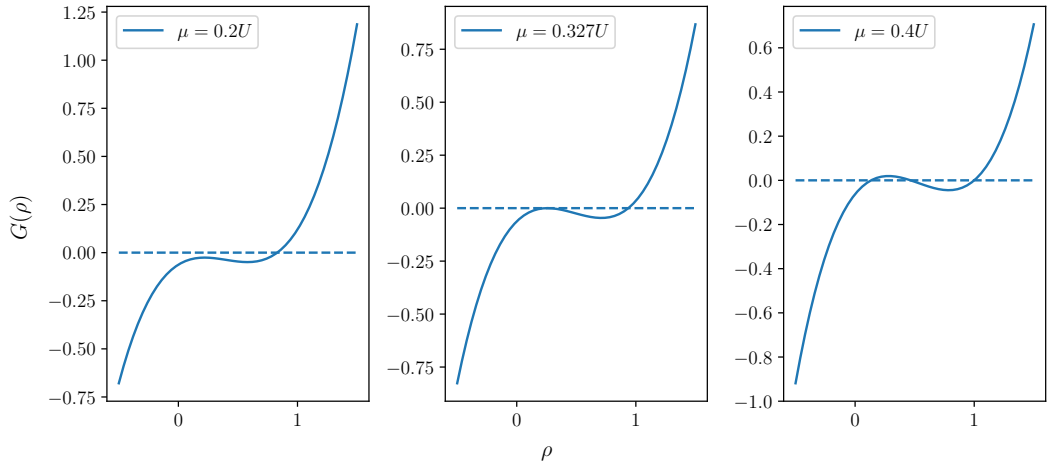

Figure 4.4: A saddle node bifurcation occurs at $\mu = \mu_1$. For values of μ less than μ_1, there is only one steady state with a high density of $\rho \sim 1$. As we increase the detuning and cross μ_1, two slightly positive roots emerge as a pair. In the context of mean-field hysteresis presented below, we observe that the smaller of these two roots is stable, while the larger root is dynamically unstable, which confirms the saddle-node nature of the bifurcation. The other parameters in $G(\rho)$ Eq. (4.18) are the same as in Figure 4.2.

$0.326775U$ and $\mu_2 = 2.379805U$. We have also plotted the function $G(\rho)$ around these two values in Figure 4.4 and Figure 4.5.

First, all real roots are also positive in both cases. For small detuning $\mu < \mu_1$ and large $\mu > \mu_2$, there are only one root, call them ρ_1 and ρ_2, respectively. ρ_1 corresponds to a high-density phase and ρ_2 corresponds to a low-density phase. Second, in the area where $< \mu_1 < \mu < \mu_2$, there are an additional root ρ_m which sits in between ρ_1 and ρ_2.

Next, we examine the stability of these solutions by simulating the dynamical hysteresis arising from a triangular modulation of the detuning μ. We consider a variation of detuning from μ_s to $\mu_s + \Delta\mu$ covering the whole range of the hysteresis in a time duration of t_s. We start at detuning and allow Eq. (4.14) to evolve over a prolonged period until a steady state is achieved. Using this steady state at the initial state, we evolve the system for time t_s while incrementing μ linearly in time until reaching $\mu_s + \Delta\mu$. Thus, $t_s/\Delta\mu$ defines the inverse of the sweep rate. We also do the same in reverse. Therefore, the total evolution time is $2t_s$. The hysteresis that persists when t_s approaches infinity is referred to as static hysteresis. This process is depicted in Figure 4.6.

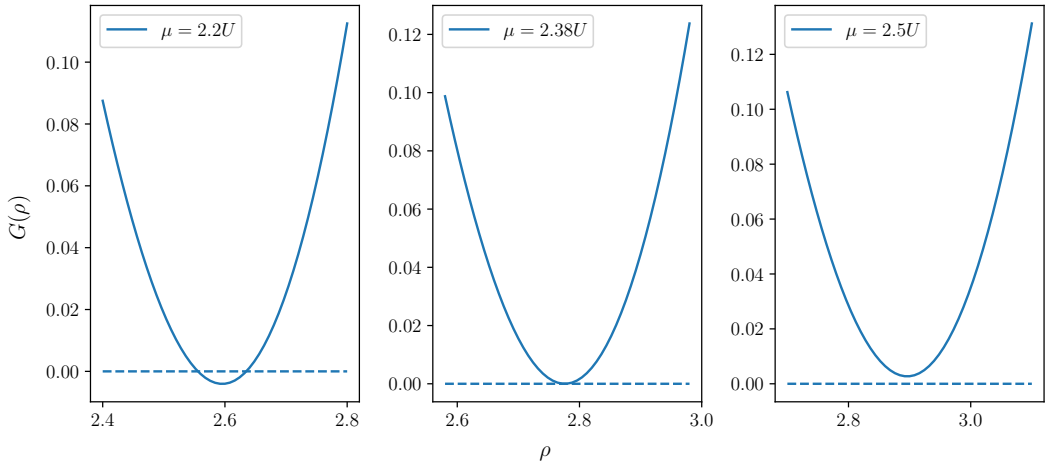

Figure 4.5: The dynamically unstable solution that arises from the first bifurcation, illustrated in Figure 4.4, moves toward the high-density stable solution as μ is increased from μ_1 to μ_2. At $\mu = \mu_2$, it collides with the high-density root, and together they disappear, indicating another saddle-node bifurcation. For $\mu > \mu_2$, bistability ceases to exist, and only one stable low-density solution remains. The other parameters in $G(\rho)$ Eq. (4.18) are the same as in Figure 4.2.

As we can see, in the region where there are three positive solutions, only two are stable, namely ρ_1 and ρ_2. They coexist for $\mu_1 < \mu < \mu_2$. At $\mu = \mu_1$ ($\mu = \mu_2$), a saddle-node bifurcation creates (annihilates) a pair of stable-unstable states.

Up to this point, we have only analyzed the mean-field equations at fixed values of the driving amplitude F, damping rate γ, and tunneling amplitude J. For the sake of completeness, we now present the mean-field phase diagrams in the $F - \mu$ plane and the $\gamma - \mu$ plane, as illustrated in Fig. 4.7.

It is evident that bistability occurs over a broad range of F and γ. In Eq. 4.14, the tunneling amplitude J is considered a redundant variable since it is equivalent to the detuning μ. As a result, we will not take J into account in this discussion.

4.3 Tensor network simulations

In this section, we will utilize the time evolution method developed in the previous chapter to simulate the dynamics of the driven-dissipative Bose-Hubbard model. We will begin by considering the Gutzwiller ansatz, which can be treated as an LPDO with matrix bond dimensions equal to one. Our findings indicate that the mean-

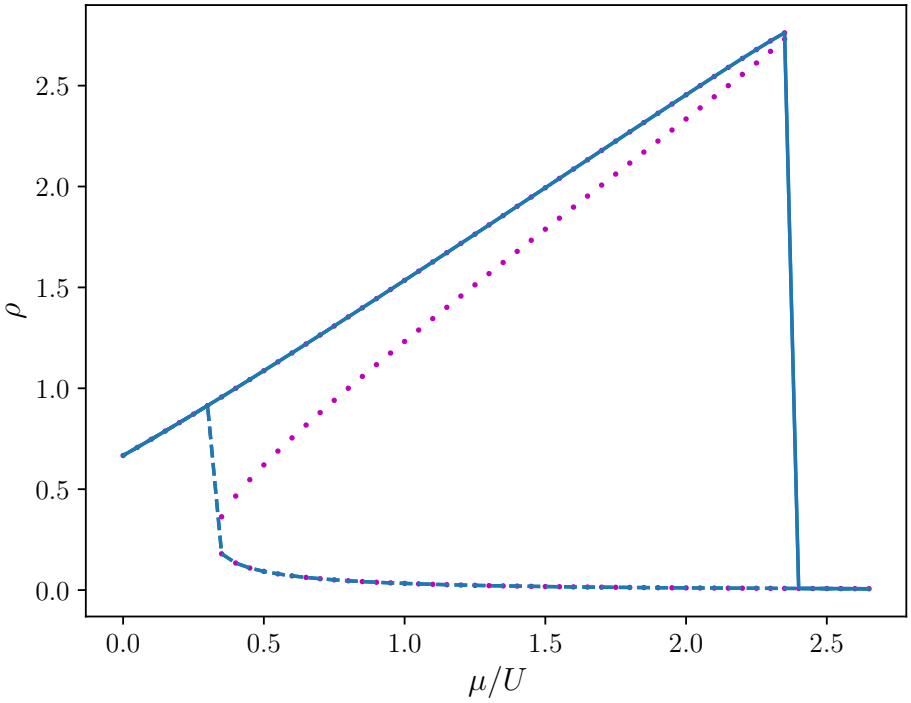

Figure 4.6: This figure illustrates that the model exhibits a bistable phase when $\mu_1 < \mu < \mu_2$, according to the Gross-Pitaevskii mean-field equation. The purple dotted line represents the solutions of $G(\rho)$. The S-shaped curve is a characteristic feature of mean-field bistability. The blue solid (dashed) lines depict the static hysteresis loop obtained by adiabatically varying μ in the increasing (decreasing) direction. The model parameters are the same as in Figure 4.2.

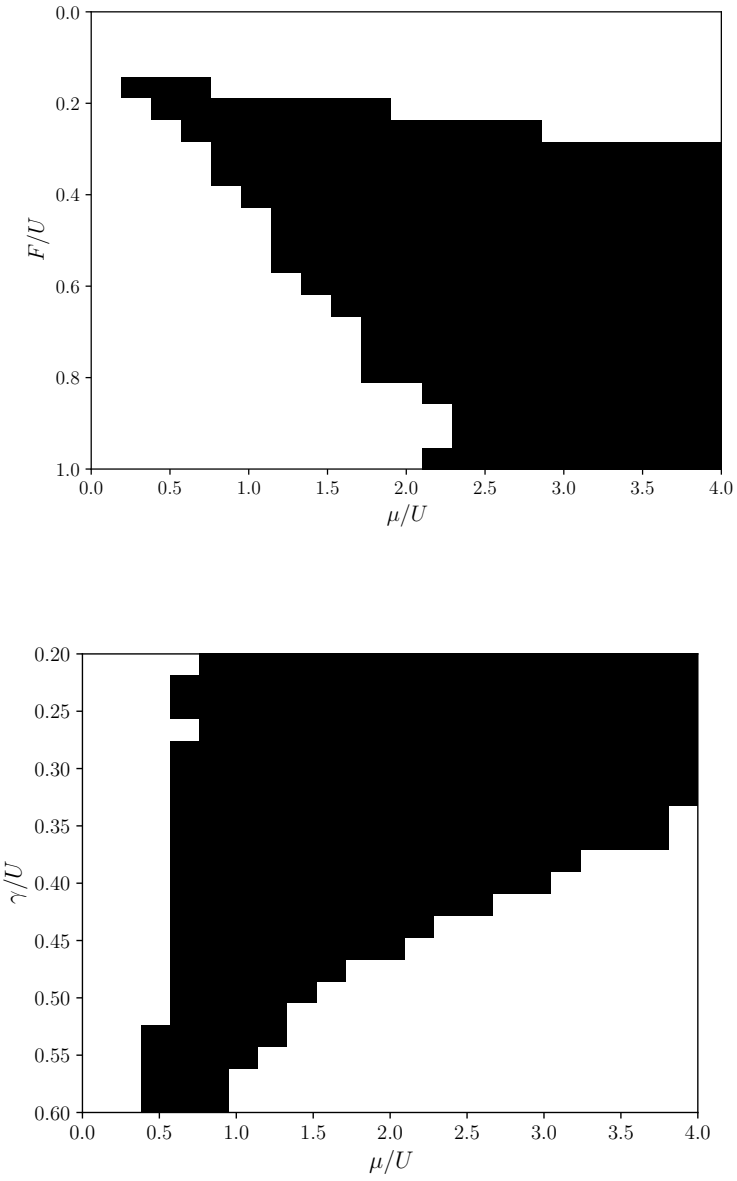

Figure 4.7: The mean-field phase diagram in the $F - \mu$ plane (top) and the $\gamma - \mu$ plane (bottom) shows the bistable region in black and the monostable region in white (transparent). In the top figure, γ is set to $0.3U$. In the bottom figure, F is set to $0.25U$.

field bistability is replaced by a first-order phase transition. The area of dynamical hysteresis exhibits a power-law decay in the fast sweep regime, while it shows an exponential decay in the slow sweep regime. Subsequently, we will present the results from the LPDO simulation, which shows that no first-order phase transition is observed, and the dynamical hysteresis area decays solely exponentially as the sweep time increases.

4.3.1 Gutzwiller ansatz

The Gross-Pitaevski mean-field equation Eq. (4.14), as discussed in the previous section, completely neglects quantum fluctuations. A more meaningful approximation is given by the Gutzwiller mean-field ansatz, expressed as follows:

$$\rho = \bigotimes_i \rho_i, \tag{4.19}$$

where ρ represents the density operator for the entire system, and ρ_i denotes the density operator at site i. Please note that from this point onward, ρ refers specifically to the density operator and should not be confused with the mean-field photon density defined in the previous section. This formulation factorizes the density operator at each site, which means that while we ignore correlations between different parts of the system, we do take into account the on-site quantum fluctuations.

One advantage of this approach is that it can be easily simulated as a tensor network with a matrix bond dimension of 1. We simulate the same dynamic hysteresis discussed in the previous section. We truncate the local Hilbert space dimension d to 4, where the results have converged. The Kraus dimension is set larger than d, such no truncation is needed. The model parameters are identical to those shown in Figure 4.2.

In Figure 4.8, we show the change of mean photon number

$$\langle n \rangle = \frac{1}{N} \mathrm{Tr} \left(\rho \sum_{i=1}^{N} n_i \right) \tag{4.20}$$

as we vary the detuning μ, where n_i is the number operator acting on the site i. N is the system size. We note that the system displays behavior significantly different from what we observed with the Gross-Pitaevski mean-field equation. Due to the strong nonlinearity, the maximum occupation $\langle n \rangle_{max}$ is approximately 1. Consequently, the hysteresis area is significantly smaller than what was shown in Figure 4.6. Notably, the hysteresis area disappears as we approach the adiabatic

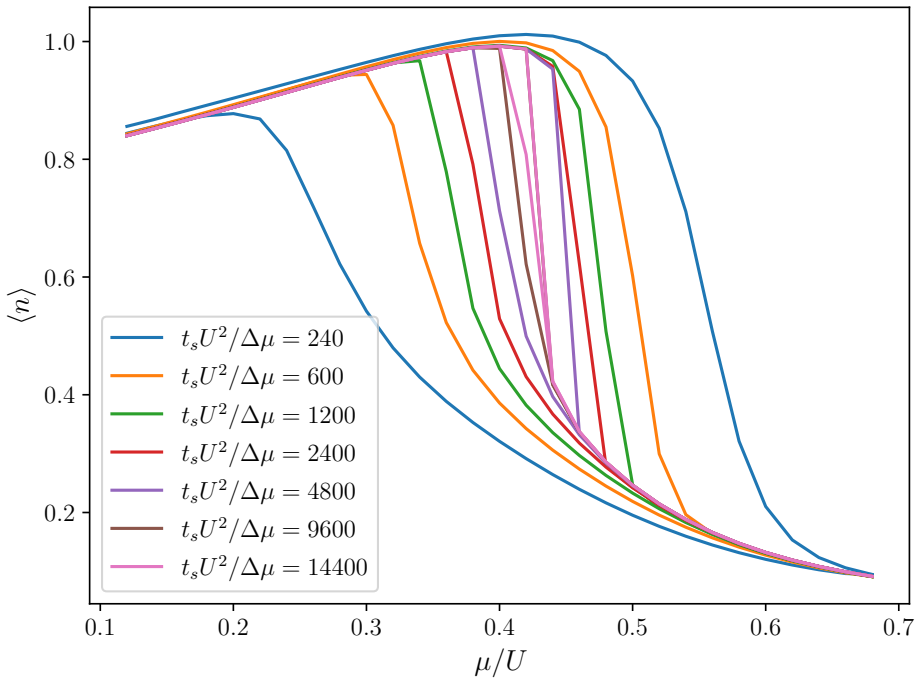

Figure 4.8: The dynamical hysteresis loop of Gutzwiller ansatz Eq. (4.19) for a system with 50 sites corresponding to different sweep times t_s (in the unit of $\Delta\mu/U^2$). For a given sweep time, the lines corresponding to higher mean photon numbers are obtained in the sweeping direction of increasing (decreasing) μ. The dynamical hysteresis disappears as $t_s \to \infty$ and leaves a sharp transition, indicating a first-order phase transition at $\mu \approx 0.43U$. The model parameters are the same as in Figure 4.2.

limit. The sharp transition at $\mu \approx 0.43U$ indicates a first-order phase transition. This contrasts sharply with the single-site model, which has an analytical solution available [26]. In that case, no phase transitions occur at finite interaction strength U.

The transition from bistability to a first-order phase transition occurs due to classical and quantum correlations. In mean-field theory, all dynamically stable solutions (local minima) have infinite lifetimes, which leads to bistability. However, when correlations are taken into account, the system can switch between the two bistable phases, resulting in a unique steady state. These switchings can be effectively captured by quantum trajectory simulations [39].

The switching time is related to the Liouvillian gap, which is defined through the eigendecomposition of the Liouvillian superoperator $\mathcal{L}$ defined in Eq. (3.1)

$$\mathcal{L}\rho = \lambda_i \rho_i, \tag{4.21}$$

where $0 = \mathrm{Re}\lambda_0 \geq \mathrm{Re}\lambda_1 \geq \cdots$. The steady state then corresponds to the eigenvector ρ_0 associated with the zero eigenvalue. The value $\mathrm{Re}\lambda_1$ represents the slowest dynamics and is referred to as the Liouvillian gap, denoted as Δ. Consequently, the switching time is inversely proportional to the Liouvillian gap, expressed as Δ^{-1}.

At the critical point in the thermodynamics limit, the gap closes ($\Delta = 0$), resulting in two degenerate steady states that correspond to the two bistable phases with both infinite lifetimes. Near the critical point, although the gap Δ is finite, it can be very small. When the timescale set by Δ^{-1} is significantly longer than other relevant timescales in the system (such as the sweep time in our example), dynamical hysteresis occurs.

We define the dynamical hysteresis area as the area enclosed in the hysteresis loop

$$A = \int \left(n^{\uparrow} - n^{\downarrow} \right) d\mu. \tag{4.22}$$

In our case, $n^{\uparrow}$ is the mean photon numbers obtained in the direction of increasing detuning μ, and $n^{\downarrow}$ is the opposite.

We present the dynamical hysteresis area A as a function of the sweep time t_s in Figures 4.9a and 4.9b. Two distinct decay patterns can be identified in the fast and slow sweep regimes, respectively. In the fast sweep regime, where the sweep time t_s is short, the area decays with sweep time t_s following a power law $A \propto t_s^{-a}$. For $N = 50$, we found that $a \approx 0.68$, as shown in Figure 4.10. This result aligns with the 2/3 power-law derived from a mean-field equation in Ref. [40]. Additionally, the agreement with mean-field theory in the fast sweep regime was also reported in Ref. [41]. At medium sweep times, a transient regime is observed for larger systems.

In the slow sweep regime, the area A decays exponentially over time and exhibits a strong finite-size effect compared to the power-law regime. This can be explained intuitively by considering the following analysis. We can express the integral as a Riemann sum for simpler notation:

$$A(t) = \sum_i \Delta\mu_i (n_i^{\uparrow}(t) - n_i^{\downarrow}(t)). \tag{4.23}$$

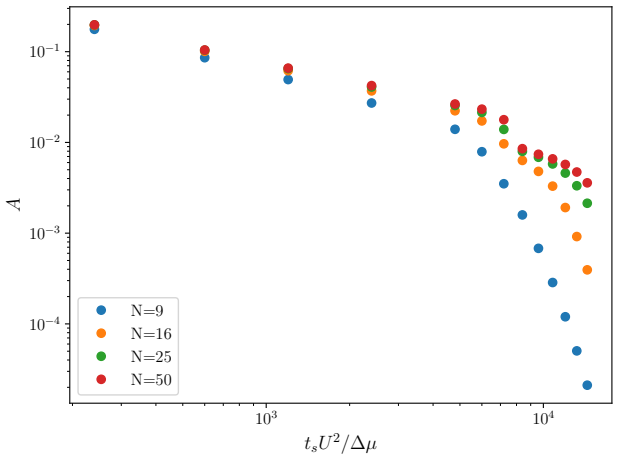

(a)

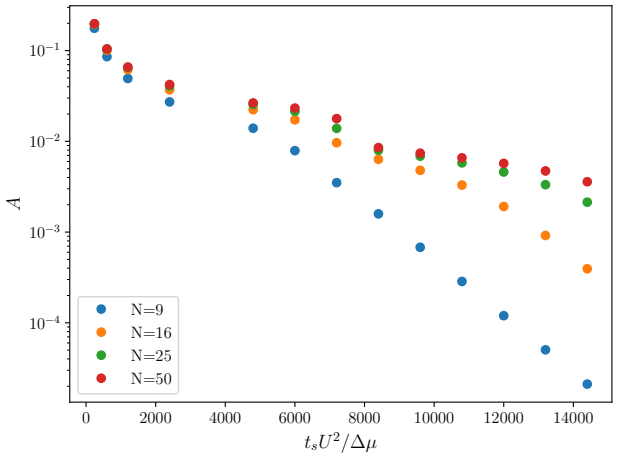

(b)

Figure 4.9: The dynamical hysteresis area A for the Gutzwiller ansatz as a function of the sweep time t_s (in the unit of $\Delta\mu/U^2$) for different system sizes N. (a) In log-log scale, the initial straight lines indicate the areas follow a power-law decay with increasing sweep time. A power-law fitting for $N = 50$ is provided in Fig. 4.10. When the sweep time is increased, the power-law decay is replaced by an exponential decay. (b) In log-linear scale. At long sweep times (towards the adiabatic limit), the area decays exponentially with a evident finite-size effect. For large system sizes, we observe a transient regime at medium sweep times. The exponential decay confirms a vanishing hysteresis area in the $t_s \to \infty$ limit. The parameters are the same as in Figure 4.2.

At large t, the mean photon numbers n_i decay exponentially

$$n_i^{\uparrow}(t) = n_i^{ss} - A_i e^{-t\Delta_i}, \tag{4.24a}$$

$$n_i^{\downarrow}(t) = n_i^{ss} + B_i e^{-t\Delta_i}, \tag{4.24b}$$

where n_i^{ss} is the mean photon number of the steady state, A_i and B_i are coefficients that depend on the system paramters. Δ_i represents the Liouvillian gap defined above. We did not include the case where $\Delta_i = 0$ at the critical point. It does not affect our analysis since it has a zero measure. Therefore, Eq. (4.23) can be written as

$$A(t) = -\sum_i \Delta\mu_i (A_i + B_i) e^{-t\Delta_i}. \tag{4.25}$$

In the slow sweep regime, the hysteresis only exists in the vicinity of the critical point. For finite systems, the Liouvillian gap Δ is always finite, even at the critical point. We anticipate that the sum Eq. (4.25) will be dominated by the term with Δ_c, the Liouvillian gap at the critical point. Hence, the area should decay exponentially. This also explains the strong finite-size effect we observed in the slow sweep regime.

4.3.2 Full quantum solution

We now present the simulation results of the full density operator as an LPDO.

First, we recall the three important parameters controlling the time evolution: the matrix bond dimension D, Kraus bond dimension K, and disentanglement steps *disent_step*. The last one determines how many time steps are computed between two disentanglement steps. The results are generally more accurate when *disent_step* is chosen small, meaning we disentangle the LPDO more frequently throughout the time evolution. However, since the disentanglement is based on an iterative algorithm, calling disentanglement too often can largely impact the performance of the algorithm. Therefore, it also requires fine-tuning.

To determine the set of parameters that yield converged results, we begin by simulating small systems ($N < 5$), where direct integration of the full density matrix remains possible. We conduct a convergence test as follows: First, we set *disent_step* $= 1$ and perform a grid search for the matrix and Kraus bond dimensions, denoted as D and K. Once we identify the sufficient sizes for D and K, we freeze these values and increase *disent_step*. Finally, we keep all parameters—D, K, and *disent_step*—fixed to compare the results across different local Hilbert space dimensions. We found that the results had already converged at a dimension of $d = 4$.

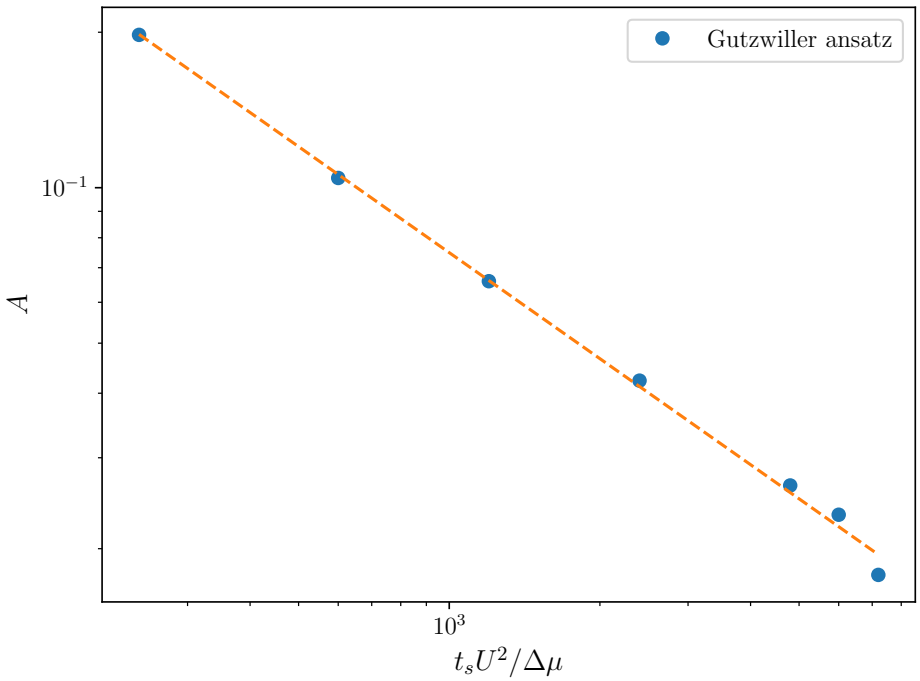

Figure 4.10: The dynamical hysteresis area A of the Gutzwiller ansatz with 50 sites as a function of the sweep time t_s in the unit of $\Delta\mu/U^2$. The dashed line is a power-law fit. In the fast sweep limit, the area A follows a power law $A \propto t_s^{-a}$ with $a \approx 0.68$, which is in great agreement with the 2/3 law found for a generic mean-field eqaution in Ref. [40]. The parameters are same as in Figure 4.2.

We repeated the same convergence test while increasing the system size until $N = 12$. We found converged results with a local Hilbert space $d = 4$, bond dimensions $D = K = 8$, and $disent\_step = 4$. These parameters are used in all subsequent simulations.

Based on the predictions of the Gutzwiller ansatz, we investigate the LPDO from two perspectives: the finite-size scaling of the order parameter $\langle n \rangle$ to determine whether a first-order phase transition is present, and the finite-time scaling of the dynamical hysteresis area, as discussed previously.

For the finite-size scaling, we evolve the systems until the hysteresis area approaches zero, allowing us to obtain the true steady states. The steady-state mean photon occupations are plotted in Figure 4.11a. We the lines intersect at $\mu \approx 0.26U$, suggesting the possibility of a first-order phase transition. However, this observation is inconclusive, as we do not observe a sudden jump in $\langle n \rangle$. Further increasing the

system size results in overlapping lines with $N = 25$, which contradicts the first-order phase transition predicted by the Gutzwiller ansatz. Figure 4.11b presents the purity of the steady states.

A similar behavior is observed in the one-dimensional lattice in Ref. [38], where the Liouvillian gap Δ decreases to a small but finite value as the lattice length increases. Consequently, the relaxation time $t_{relax} = 1/\Delta$ becomes very long, leading to dynamical hysteresis.

In Figure 4.12, we present the dynamical hysteresis of a LPDO with 25 sites. Unlike in Figure 4.8, the discontinuity in the mean photon number $\langle n \rangle$ is absent in Figure 4.12. This observation indicates that the first-order phase transition seen in the Gutzwiller ansatz has been smoothed out when taking into account the correlations between different parts of the system.

In Figure 4.13, we show the dynamical hysteresis area as a function of sweep time t_s. Once again, we observe significant differences compared to the Gutzwiller ansatz. For the LPDO, the dynamical hysteresis area demonstrates only an exponential decay with respect to the sweep time t_s:

$$A \propto e^{at_s},$$

with the exponent $a \approx -8 \times 10^{-4} U$. It is important to note that the sweep times in Figure 4.12 belong to the fast sweep regime for the Gutzwiller ansatz, see Figure 4.8. Therefore, the absence of power law is confirmed.

Based on our analysis from Eq. (4.23) to Eq. (4.25), the exponent a is expected to be related to the Liouvillian gap $\Delta = -a$, suggesting a nearly vanishing gap. However, as seen in Figures 4.11a and 4.12, there is no abrupt jump in the order parameter $\langle n \rangle$. This intriguing behavior warrants further investigation in our upcoming research. Simulation of larger system sizes are needed to confirm if the gap indeed vanishes in the thermodynamic limit.

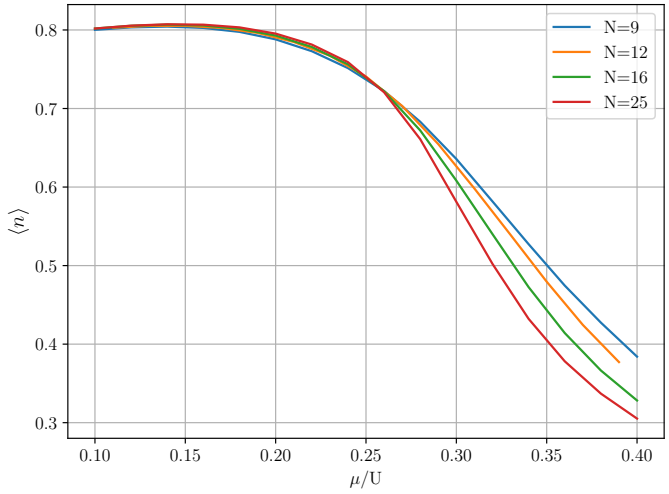

(a)

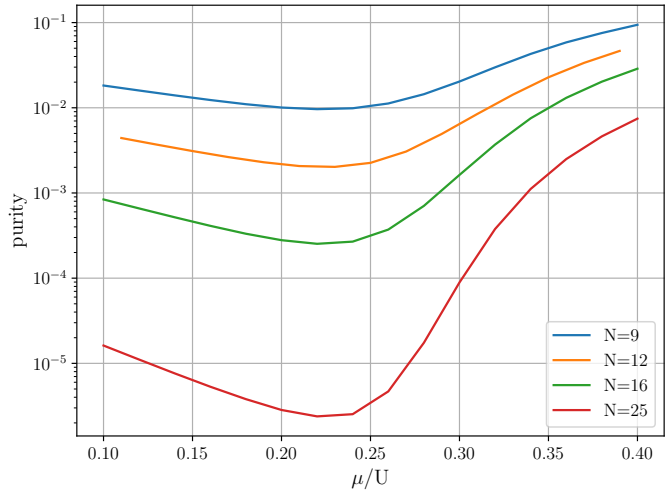

(b)

Figure 4.11: Finite-size scaling for the driven-dissipative Bose-Hubbard model (a) The steady-state mean photon number $\langle n \rangle$. A crossing at around $\mu = 0.26U$ suggests a critical point for the first-order phase transition. However, further increasing system size shows overlapping lines with $N = 25$, meaning no sharp transition exists. (b) The purity of the steady states. The high occupation phase is more mixed. At large detuning, the purity approaches one as the system approaches the vacuum. The parameters are the same in Figure 4.2.

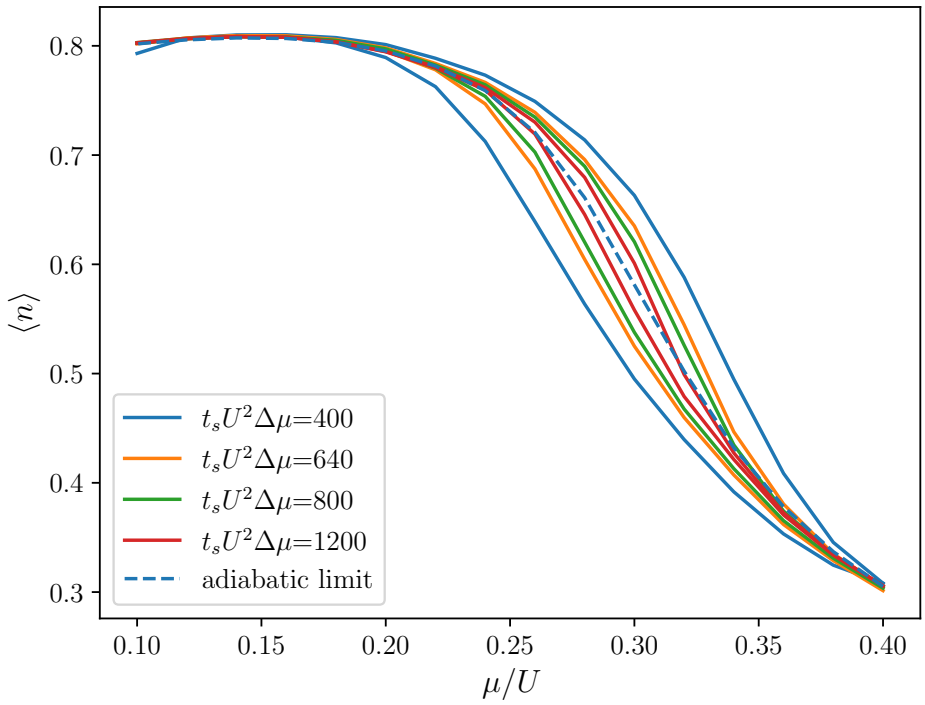

Figure 4.12: The dynamical hysteresis loop of a full LPDO for a system with 25 sites corresponding to different sweep times t_s (in the unit of $\Delta\mu/U^2$). The dashed line, which corresponds to the solid red line in Figure 4.11a, is obtained by evolving the system for a prolonged time until no hysteresis is observed. The mean photon occupation $\langle n \rangle$ changes smoothly with the detuning μ. Therefore, no first-order phase transition is observed, which contrasts with the predictions of the Gutzwiller ansatz. The model parameters are the same as in Figure 4.2.

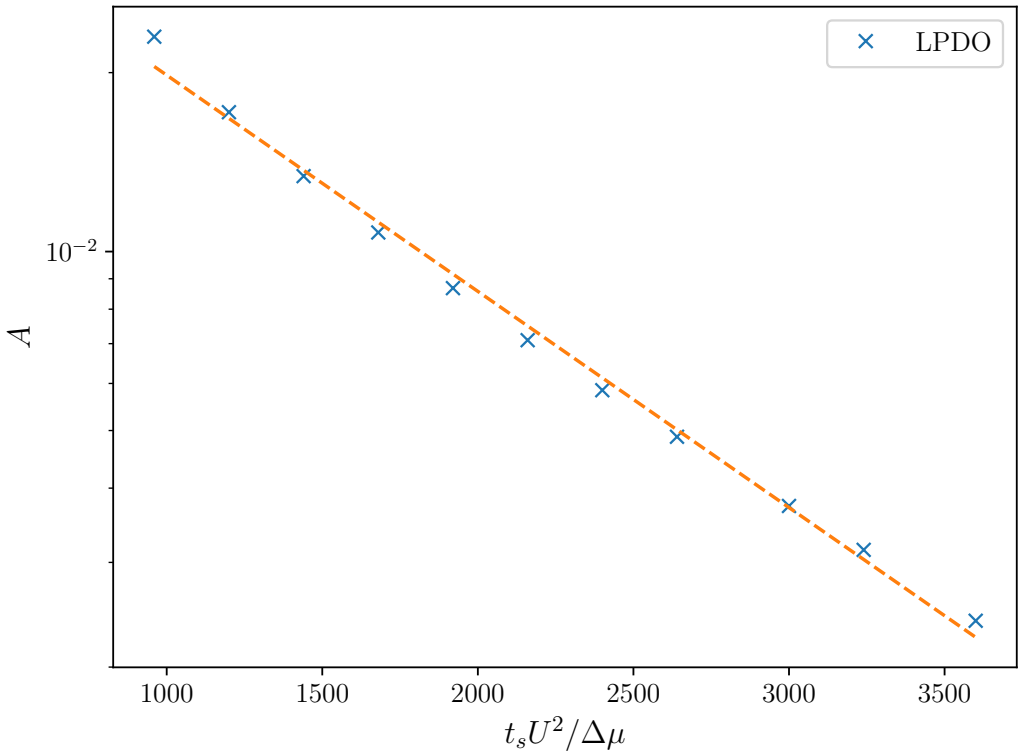

Figure 4.13: The dynamical hysteresis area A for the full LPDO as a function of sweep time t_s (in units of $\Delta\mu/U^2$). The dashed line is exponential fit $A \propto e^{at_s}$ with the exponent $a \approx -8 \times 10^{-4} U$. The sweep times in this plot belong to the fast sweep regime for the Gutzwiller ansatz (see Figure 4.8), where the area decays as a power-law of the sweep time t_s. The model parameters are the same as in Figure. 4.2.

Chapter 5

Summary and outlook

In the first part of the thesis, we extended current methods for simulating one-dimensional open quantum systems using tensor networks. We employed a locally purified density operator, which is positive semi-definite by construction. This approach utilized a variational method to simulate the dynamics of the density operator according to the Lindblad equation. This method has the advantage of preserving the unit trace and the positivity of the density operator at all times. By utilizing a disentanglement procedure, we reduced the algorithm's complexity significantly and allowed for long-time dynamics simulation.

In the second part, we systematically studied the driven-dissipative Bose-Hubbard model in the strong interaction regime, which was intractable with other methods. We demonstrated that the model exhibits mean-field bistability. Next, we simulated the time evolution, where the Gutzwiller ansatz predicts a first-order phase transition and a power-law decay of the dynamical hysteresis area in the fast sweep regime before transitioning to exponential decay. Finally, we simulated the full locally purified density operator (LPDO). After applying finite-size scaling, we found that the first-order phase transition is smoothed out due to the correlations between different parts of the system. The dynamical hysteresis area exhibits only an exponential decay.

For future research, one could study the relationship between the bond dimensions in LPDO and the physical properties of the state, such as purity and entanglement of formation [42]. Based on this analysis, one may be able to propose an improved ansatz for representing a density operator with tensor networks. Furthermore, we can investigate the effectiveness of this method in various open quantum many-body systems and compare it to other approaches, such as the variational approach in Ref. [28]. Given that our method inherently preserves a positive density matrix, this comparison could help classify models where positivity is of greater significance.

Appendix A

Fourier transform of the driven-dissipative Bose-Hubbard model

In the main text, we considered only the case where the driving in the driven-dissipative Bose-Hubbard model is homogeneous. In Fourier space, this means we are only driving the $k = 0$ mode [43].

Consider the Fourier expansion of the annihilation operator,

$$\hat{b}_j = \frac{1}{\sqrt{N}} \sum_k \hat{b}_k e^{ikja}, \quad \hat{b}_j^\dagger = \frac{1}{\sqrt{N}} \sum_k \hat{b}_k^\dagger e^{-ikja} \tag{A.1}$$

where a is the lattice spacing. The Hamiltonian Eq. (4.9) in the Fourier space thus reads

$$\begin{aligned} \hat{H}_k = &-\Delta \sum_k \hat{b}_k^\dagger \hat{b}_k - \frac{J}{N} \sum_{\langle j,l \rangle} 2\cos\left(k\left(j-l\right)\right) \hat{b}_k^\dagger \hat{b}_k \\ &+ \frac{F}{\sqrt{N}} \sum_{j,k} \left(\hat{b}_k^\dagger e^{-ikja} + \hat{b}_k e^{ikja} \right) \\ &+ \frac{U}{2N} \sum_{k_1,k_2,k_3} \hat{b}_{k_1}^\dagger \hat{b}_{k_2}^\dagger \hat{b}_{k_3} \hat{b}_{k_1+k_2-k_3} \end{aligned} \tag{A.2}$$

We observe that the driving term vanishes for $k \neq 0$, meaning that only the $k = 0$ mode is externally driven. Additionally, only the last term mixes different Fourier modes. If we ignore the nonlinear scattering between different modes, only the $k = 0$ mode will be populated. In this scenario, the model becomes uncoupled and can be mapped as a single Kerr cavity.

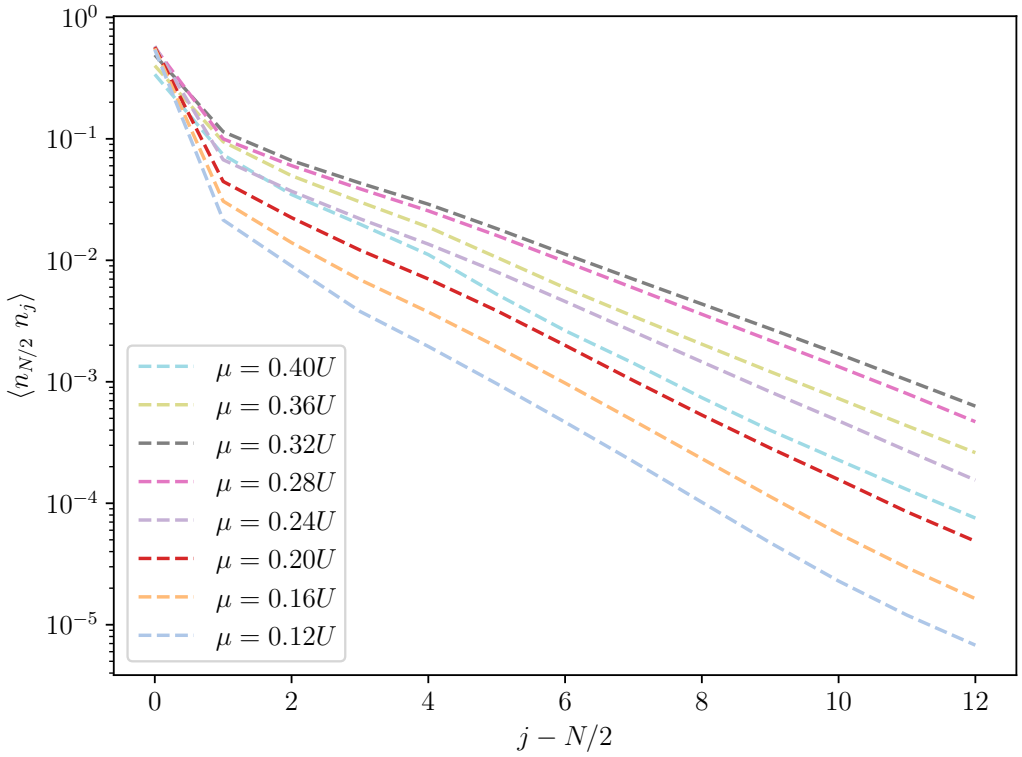

Figure A.1: The connected density-density correlation function for different values of dtuning. The It is clear that the correlation decays exponentially in all cases.

$$\hat{H} = \omega_0 \hat{b}_0^\dagger \hat{b}_0 + F_{eff}\left(\hat{b}_0^\dagger + \hat{b}_0\right) + \frac{U_{eff}}{2}\hat{b}_0^\dagger \hat{b}_0^\dagger \hat{b}_0 \hat{b}_0$$

where $\omega_0 = -\mu - 2J$, $F_{eff} = \sqrt{N}F$, and $U_{eff} = U/N$. In this case, we can directly approach the thermodynamic limit by letting $F_{eff} \to \infty$ and $U_{eff} \to 0$ while keeping $U_{eff}F_{eff}^2$ constant.

One direct consequence of ignoring the higher k modes is that the system would be perfectly correlated, implying that the correlation function would be constant. However, as shown in Figure A.1, the correlation in our system decays exponentially. Thus, the mapping is not valid. This outcome is expected, given that in our parameter regime, nonlinearity is dominant.

Bibliography

[1] Ulrich Schollwöck. 'The density-matrix renormalization group in the age of matrix product states'. In: *Annals of Physics* 326.1 (Jan. 2011), pp. 96–192. ISSN: 0003-4916. DOI: 10.1016/j.aop.2010.09.012. URL: http://dx.doi.org/10.1016/j.aop.2010.09.012.

[2] Guifré Vidal. 'Efficient Classical Simulation of Slightly Entangled Quantum Computations'. In: *Phys. Rev. Lett.* 91 (14 Oct. 2003), p. 147902. DOI: 10.1103/PhysRevLett.91.147902. URL: https://link.aps.org/doi/10.1103/PhysRevLett.91.147902.

[3] Guifré Vidal. 'Efficient Simulation of One-Dimensional Quantum Many-Body Systems'. In: *Phys. Rev. Lett.* 93 (4 July 2004), p. 040502. DOI: 10.1103/PhysRevLett.93.040502. URL: https://link.aps.org/doi/10.1103/PhysRevLett.93.040502.

[4] Jutho Haegeman et al. 'Unifying time evolution and optimization with matrix product states'. In: *Phys. Rev. B* 94 (16 Oct. 2016), p. 165116. DOI: 10.1103/PhysRevB.94.165116. URL: https://link.aps.org/doi/10.1103/PhysRevB.94.165116.

[5] F. Verstraete, J. J. García-Ripoll and J. I. Cirac. 'Matrix Product Density Operators: Simulation of Finite-Temperature and Dissipative Systems'. In: *Phys. Rev. Lett.* 93 (20 Nov. 2004), p. 207204. DOI: 10.1103/PhysRevLett.93.207204. URL: https://link.aps.org/doi/10.1103/PhysRevLett.93.207204.

[6] A. H. Werner et al. 'Positive Tensor Network Approach for Simulating Open Quantum Many-Body Systems'. In: *Phys. Rev. Lett.* 116 (23 June 2016), p. 237201. DOI: 10.1103/PhysRevLett.116.237201. URL: https://link.aps.org/doi/10.1103/PhysRevLett.116.237201.

[7] Hendrik Weimer, Augustine Kshetrimayum and Román Orús. 'Simulation methods for open quantum many-body systems'. In: *Rev. Mod. Phys.* 93 (1 Mar. 2021), p. 015008. DOI: 10.1103/RevModPhys.93.015008. URL: https://link.aps.org/doi/10.1103/RevModPhys.93.015008.

[8] Johannes Hauschild et al. 'Finding purifications with minimal entanglement'. In: *Phys. Rev. B* 98 (23 Dec. 2018), p. 235163. DOI: 10.1103/PhysRevB.98.235163. URL: https://link.aps.org/doi/10.1103/PhysRevB.98.235163.

[9] Michael A. Nielsen and Isaac L. Chuang. *Quantum Computation and Quantum Information: 10th Anniversary Edition*. Cambridge University Press, 2010.

[10] Mark M. Wilde. *Quantum Information Theory*. Cambridge University Press, 2013.

[11] Don N. Page. 'Average entropy of a subsystem'. In: *Phys. Rev. Lett.* 71 (9 Aug. 1993), pp. 1291–1294. DOI: 10.1103/PhysRevLett.71.1291. URL: https://link.aps.org/doi/10.1103/PhysRevLett.71.1291.

[12] J. Eisert, M. Cramer and M. B. Plenio. 'Colloquium: Area laws for the entanglement entropy'. In: *Rev. Mod. Phys.* 82 (1 Feb. 2010), pp. 277–306. DOI: 10.1103/RevModPhys.82.277. URL: https://link.aps.org/doi/10.1103/RevModPhys.82.277.

[13] M B Hastings. 'An area law for one-dimensional quantum systems'. In: *Journal of Statistical Mechanics: Theory and Experiment* 2007.08 (Aug. 2007), P08024–P08024. ISSN: 1742-5468. DOI: 10.1088/1742-5468/2007/08/p08024. URL: http://dx.doi.org/10.1088/1742-5468/2007/08/P08024.

[14] Leonid Gurvits. 'Classical deterministic complexity of Edmonds' Problem and quantum entanglement'. In: *Proceedings of the Thirty-Fifth Annual ACM Symposium on Theory of Computing*. STOC '03. San Diego, CA, USA: Association for Computing Machinery, 2003, pp. 10–19. ISBN: 1581136749. DOI: 10.1145/780542.780545. URL: https://doi.org/10.1145/780542.780545.

[15] Ryszard Horodecki et al. 'Quantum entanglement'. In: *Rev. Mod. Phys.* 81 (2 June 2009), pp. 865–942. DOI: 10.1103/RevModPhys.81.865. URL: https://link.aps.org/doi/10.1103/RevModPhys.81.865.

[16] Charles H. Bennett et al. 'Mixed-state entanglement and quantum error correction'. In: *Phys. Rev. A* 54 (5 Nov. 1996), pp. 3824–3851. DOI: 10.1103/PhysRevA.54.3824. URL: https://link.aps.org/doi/10.1103/PhysRevA.54.3824.

[17] William K. Wootters. 'Entanglement of Formation of an Arbitrary State of Two Qubits'. In: *Phys. Rev. Lett.* 80 (10 Mar. 1998), pp. 2245–2248. DOI: 10.1103/PhysRevLett.80.2245. URL: https://link.aps.org/doi/10.1103/PhysRevLett.80.2245.

[18] Barbara M. Terhal et al. 'The entanglement of purification'. In: *Journal of Mathematical Physics* 43.9 (Sept. 2002), pp. 4286–4298. ISSN: 0022-2488. DOI: 10.1063/1.1498001. eprint: https://pubs.aip.org/aip/jmp/article-pdf/43/9/4286/19183123/4286_1_online.pdf. URL: https://doi.org/10.1063/1.1498001.

[19] Jan Bouda and Vladimír Bu žek. 'Purification and correlated measurements of bipartite mixed states'. In: *Phys. Rev. A* 65 (3 Feb. 2002), p. 034304. DOI: 10.1103/PhysRevA.65.034304. URL: https://link.aps.org/doi/10.1103/PhysRevA.65.034304.

[20] M. Kliesch, D. Gross and J. Eisert. 'Matrix-Product Operators and States: NP-Hardness and Undecidability'. In: *Phys. Rev. Lett.* 113 (16 Oct. 2014), p. 160503. DOI: 10.1103/PhysRevLett.113.160503. URL: https://link.aps.org/doi/10.1103/PhysRevLett.113.160503.

[21] Man-Duen Choi. 'Completely positive linear maps on complex matrices'. In: *Linear Algebra and its Applications* 10.3 (1975), pp. 285–290. ISSN: 0024-3795. DOI: https://doi.org/10.1016/0024-3795(75)90075-0. URL: https://www.sciencedirect.com/science/article/pii/0024379575900750.

[22] G. Lindblad. 'On the generators of quantum dynamical semigroups'. In: *Communications in Mathematical Physics* 48.2 (June 1976), pp. 119–130. ISSN: 1432-0916. DOI: 10.1007/BF01608499. URL: https://doi.org/10.1007/BF01608499.

[23] Vittorio Gorini, Andrzej Kossakowski and E. C. G. Sudarshan. 'Completely positive dynamical semigroups of N-level systems'. In: *Journal of Mathematical Physics* 17.5 (May 1976), pp. 821–825. ISSN: 0022-2488. DOI: 10.1063/1.522979. eprint: https://pubs.aip.org/aip/jmp/article-pdf/17/5/821/19090720/821_1_online.pdf. URL: https://doi.org/10.1063/1.522979.

[24] Daniel Manzano. 'A short introduction to the Lindblad master equation'. In: *AIP Advances* 10.2 (Feb. 2020), p. 025106. ISSN: 2158-3226. DOI: 10.1063/1.5115323. eprint: https://pubs.aip.org/aip/adv/article-pdf/doi/10.1063/1.5115323/12881278/025106_1_online.pdf. URL: https://doi.org/10.1063/1.5115323.

[25] David E Evans and Harald Hanche-Olsen. 'The generators of positive semigroups'. In: *Journal of Functional Analysis* 32.2 (1979), pp. 207–212. ISSN: 0022-1236. DOI: https://doi.org/10.1016/0022-1236(79)90054-5. URL: https://www.sciencedirect.com/science/article/pii/0022123679900545.

[26] P D Drummond and D F Walls. 'Quantum theory of optical bistability. I. Nonlinear polarisability model'. In: *Journal of Physics A: Mathematical and General* 13.2 (Feb. 1980), p. 725. DOI: 10.1088/0305-4470/13/2/034. URL: https://dx.doi.org/10.1088/0305-4470/13/2/034.

[27] Toma ž Prosen. 'Exact Nonequilibrium Steady State of a Strongly Driven Open XXZ Chain'. In: *Phys. Rev. Lett.* 107 (13 Sept. 2011), p. 137201. DOI: 10.1103/PhysRevLett.107.137201. URL: https://link.aps.org/doi/10.1103/PhysRevLett.107.137201.

[28] Jian Cui, J. Ignacio Cirac and Mari Carmen Bañuls. 'Variational Matrix Product Operators for the Steady State of Dissipative Quantum Systems'. In: *Phys. Rev. Lett.* 114 (22 June 2015), p. 220601. DOI: 10.1103/PhysRevLett.114.220601. URL: https://link.aps.org/doi/10.1103/PhysRevLett.114.220601.

[29] Hendrik Weimer. 'Variational Principle for Steady States of Dissipative Quantum Many-Body Systems'. In: *Phys. Rev. Lett.* 114 (4 Jan. 2015), p. 040402. DOI: 10.1103/PhysRevLett.114.040402. URL: https://link.aps.org/doi/10.1103/PhysRevLett.114.040402.

[30] Iacopo Carusotto and Cristiano Ciuti. 'Spontaneous microcavity-polariton coherence across the parametric threshold: Quantum Monte Carlo studies'. In: *Phys. Rev. B* 72 (12 Sept. 2005), p. 125335. DOI: 10.1103/PhysRevB.72.125335. URL: https://link.aps.org/doi/10.1103/PhysRevB.72.125335.

[31] Andrew J. Daley. 'Quantum trajectories and open many-body quantum systems'. In: *Advances in Physics* 63.2 (2014), pp. 77–149. DOI: 10.1080/00018732.2014.933502. eprint: https://doi.org/10.1080/00018732.2014.933502. URL: https://doi.org/10.1080/00018732.2014.933502.

[32] Alexandre Blais et al. 'Circuit quantum electrodynamics'. In: *Rev. Mod. Phys.* 93 (2 May 2021), p. 025005. DOI: 10.1103/RevModPhys.93.025005. URL: https://link.aps.org/doi/10.1103/RevModPhys.93.025005.

[33] Iacopo Carusotto and Cristiano Ciuti. 'Quantum fluids of light'. In: *Rev. Mod. Phys.* 85 (1 Feb. 2013), pp. 299–366. DOI: 10.1103/RevModPhys.85.299. URL: https://link.aps.org/doi/10.1103/RevModPhys.85.299.

[34] Sebastian Diehl et al. 'Dynamical Phase Transitions and Instabilities in Open Atomic Many-Body Systems'. In: *Phys. Rev. Lett.* 105 (1 July 2010), p. 015702. DOI: 10.1103/PhysRevLett.105.015702. URL: https://link.aps.org/doi/10.1103/PhysRevLett.105.015702.

[35] Fabrizio Minganti et al. 'Spectral theory of Liouvillians for dissipative phase transitions'. In: *Phys. Rev. A* 98 (4 Oct. 2018), p. 042118. DOI: 10.1103/PhysRevA.98.042118. URL: https://link.aps.org/doi/10.1103/PhysRevA.98.042118.

[36] Alexandre Le Boité, Giuliano Orso and Cristiano Ciuti. 'Steady-State Phases and Tunneling-Induced Instabilities in the Driven Dissipative Bose-Hubbard Model'. In: *Phys. Rev. Lett.* 110 (23 June 2013), p. 233601. DOI: 10.1103/PhysRevLett.110.233601. URL: https://link.aps.org/doi/10.1103/PhysRevLett.110.233601.

[37] Mattias Fitzpatrick et al. 'Observation of a Dissipative Phase Transition in a One-Dimensional Circuit QED Lattice'. In: *Phys. Rev. X* 7 (1 Feb. 2017), p. 011016. DOI: 10.1103/PhysRevX.7.011016. URL: https://link.aps.org/doi/10.1103/PhysRevX.7.011016.

[38] Filippo Vicentini et al. 'Critical slowing down in driven-dissipative Bose-Hubbard lattices'. In: *Phys. Rev. A* 97 (1 Jan. 2018), p. 013853. DOI: 10.1103/PhysRevA.97.013853. URL: https://link.aps.org/doi/10.1103/PhysRevA.97.013853.

[39] Matteo Biondi et al. 'Nonequilibrium gas-liquid transition in the driven-dissipative photonic lattice'. In: *Phys. Rev. A* 96 (4 Oct. 2017), p. 043809. DOI: 10.1103/PhysRevA.96.043809. URL: https://link.aps.org/doi/10.1103/PhysRevA.96.043809.

[40] Peter Jung et al. 'Scaling law for dynamical hysteresis'. In: *Phys. Rev. Lett.* 65 (15 Oct. 1990), pp. 1873–1876. DOI: 10.1103/PhysRevLett.65.1873. URL: https://link.aps.org/doi/10.1103/PhysRevLett.65.1873.

[41] W. Casteels et al. 'Power laws in the dynamic hysteresis of quantum nonlinear photonic resonators'. In: *Phys. Rev. A* 93 (3 Mar. 2016), p. 033824. DOI: 10.1103/PhysRevA.93.033824. URL: https://link.aps.org/doi/10.1103/PhysRevA.93.033824.

[42] Luigi Amico et al. 'Entanglement in many-body systems'. In: *Rev. Mod. Phys.* 80 (2 May 2008), pp. 517–576. DOI: 10.1103/RevModPhys.80.517. URL: https://link.aps.org/doi/10.1103/RevModPhys.80.517.

[43] W. Casteels, R. Fazio and C. Ciuti. 'Critical dynamical properties of a first-order dissipative phase transition'. In: *Phys. Rev. A* 95 (1 Jan. 2017), p. 012128. DOI: 10.1103/PhysRevA.95.012128. URL: https://link.aps.org/doi/10.1103/PhysRevA.95.012128.